Article

Developmental Cell

Interferon-γ resistance and immune evasion in glioma develop via Notch-regulated co-evolution of malignant and immune cells

Graphical abstract

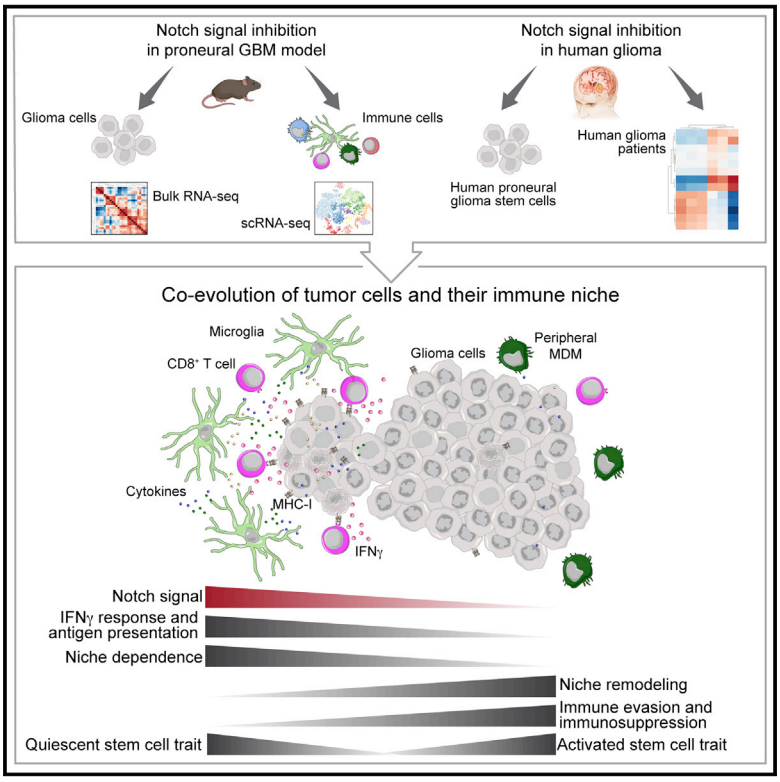

Highlights

- Tumor cells and their immune niche co-evolve during tumor initiation
- Proneural glioma cells evade immune niche control by lowering Notch activity
- IFNγ response and MHC-I expression by GSCs are co-regulated by Notch
- A single pathway governs glioma immunophenotype and activated cancer stem cell traits

Authors

Elena Parmigiani, Robert Ivanek, Chiara Rolando, ..., Roxane Tussiwand, Verdon Taylor, Claudio Giachino

Correspondence

claudio.giachino@unibas.ch

In brief

Parmigiani et al. demonstrate that Notch signaling regulates the interferon-γ response of glioma cells and recruitment of immune cells to the tumor. Uncoupling of immune and tumor cells by Notch inhibition favors an immunosuppressive microenvironment, exacerbates immune evasion, and promotes activated stem-cell-driven, niche-independent glioma growth.

Parmigiani et al., 2022, Developmental Cell 57, 1847–1865
August 8, 2022
https://doi.org/10.1016/j.devcel.2022.06.006

CellPress

Developmental Cell

CellPress
OPEN ACCESS

Article

Interferon-γ resistance and immune evasion in glioma develop via Notch-regulated co-evolution of malignant and immune cells

Elena Parmigiani,[1] Robert Ivanek,[2,3] Chiara Rolando,[1,17] Katrin Hafen,[4] Gleb Turchinovich,[5,6] Frank Michael Lehmann,[5,6] Alexandra Gerber,[7] Sime Brkic,[8] Stephan Frank,[9] Sara C. Meyer,[8,10] Hiroaki Wakimoto,[11] Murat Günel,[12] Angeliki Louvi,[12] Luigi Mariani,[13] Daniela Finke,[5,6] Georg Holländer,[4,14,15] Gregor Hutter,[7,13] Roxane Tussiwand,[16,18] Verdon Taylor,[1] and Claudio Giachino[1,19,*]

[1]Embryology and Stem Cell Biology, Department of Biomedicine, University of Basel, Mattenstrasse 28, 4058 Basel, Switzerland
[2]Swiss Institute of Bioinformatics, Hebelstrasse 20, 4031 Basel, Switzerland
[3]Bioinformatics Core Facility, Department of Biomedicine, University of Basel, Hebelstrasse 20, 4031 Basel, Switzerland
[4]Pediatric Immunology, Department of Biomedicine, University of Basel, Mattenstrasse 28, 4058 Basel, Switzerland
[5]Developmental Immunology, Department of Biomedicine, University of Basel, Mattenstrasse 28, 4058 Basel, Switzerland
[6]University Children's Hospital of Basel, University of Basel, Spitalstrasse 33, 4056, Basel, Switzerland
[7]Brain Tumor Immunotherapy, Department of Biomedicine, University of Basel, Hebelstrasse 20, 4031 Basel, Switzerland
[8]Department of Biomedicine, University Hospital Basel and University of Basel, Hebelstrasse 20, 4031 Basel, Switzerland
[9]Division of Neuropathology, Institute of Pathology, University of Basel, Schoenbeinstrasse 40, 4031 Basel, Switzerland
[10]Division of Hematology, University Hospital Basel, Petersgraben 4, 4031 Basel, Switzerland
[11]Department of Neurosurgery, Massachusetts General Hospital and Harvard Medical School, Boston, MA 02114, USA
[12]Department of Neurosurgery, Yale School of Medicine, New Haven, CT 06520-8082, USA
[13]Department of Neurosurgery, University Hospital Basel, Petersgraben 4, 4031 Basel, Switzerland
[14]Weatherall Institute of Molecular Medicine and Department of Paediatrics, University of Oxford, Oxford OX3 9DU, UK
[15]Department of Biosystems Science and Engineering, ETH Zurich, Mattenstrasse 26, 4058 Basel, Switzerland
[16]Immune Regulation, Department of Biomedicine, University of Basel, Mattenstrasse 28, 4058 Basel, Switzerland
[17]Present address: Clinical Next-Generation Sequencing, Specialty Diagnostics Group, Thermo Fisher Scientific, Via Tiepolo 18, Monza 20900, Italy
[18]Present address: National Institute of Dental and Craniofacial Research, NIH, Bethesda, MD 20892, USA
[19]Lead contact
*Correspondence: claudio.giachino@unibas.ch
https://doi.org/10.1016/j.devcel.2022.06.006

SUMMARY

Immune surveillance is critical to prevent tumorigenesis. Gliomas evade immune attack, but the underlying mechanisms remain poorly understood. We show that glioma cells can sustain growth independent of immune system constraint by reducing Notch signaling. Loss of Notch activity in a mouse model of glioma impairs MHC-I and cytokine expression and curtails the recruitment of anti-tumor immune cell populations in favor of immunosuppressive tumor-associated microglia/macrophages (TAMs). Depletion of T cells simulates Notch inhibition and facilitates tumor initiation. Furthermore, Notch-depleted glioma cells acquire resistance to interferon-γ and TAMs re-educating therapy. Decreased interferon response and cytokine expression by human and mouse glioma cells correlate with low Notch activity. These effects are paralleled by upregulation of oncogenes and downregulation of quiescence genes. Hence, suppression of Notch signaling enables gliomas to evade immune surveillance and increases aggressiveness. Our findings provide insights into how brain tumor cells shape their microenvironment to evade immune niche control.

INTRODUCTION

Local feedback between stem cells and their niche tightly controls cell fate in healthy tissues. In tumors, however, cancer stem cells can coerce their niche to support uncontrolled growth of malignant cells, profoundly influencing therapeutic efficacy (Prager et al., 2019). Immune cells have emerged as prominent components of stem cell niches and effectors of stem cell behavior during both homeostasis and tumor formation (Binnewies et al., 2018; Naik et al., 2018; Prager et al., 2019). Our understanding of how cancer stem cells influence evolution of the tumor microenvironment (TME) and build their immune niche is limited. Decoding the processes that translate into a survival advantage for cancer cells under immune selection pressure is fundamental to understand immune evasion and develop effective treatments. Filling these gaps in our knowledge is

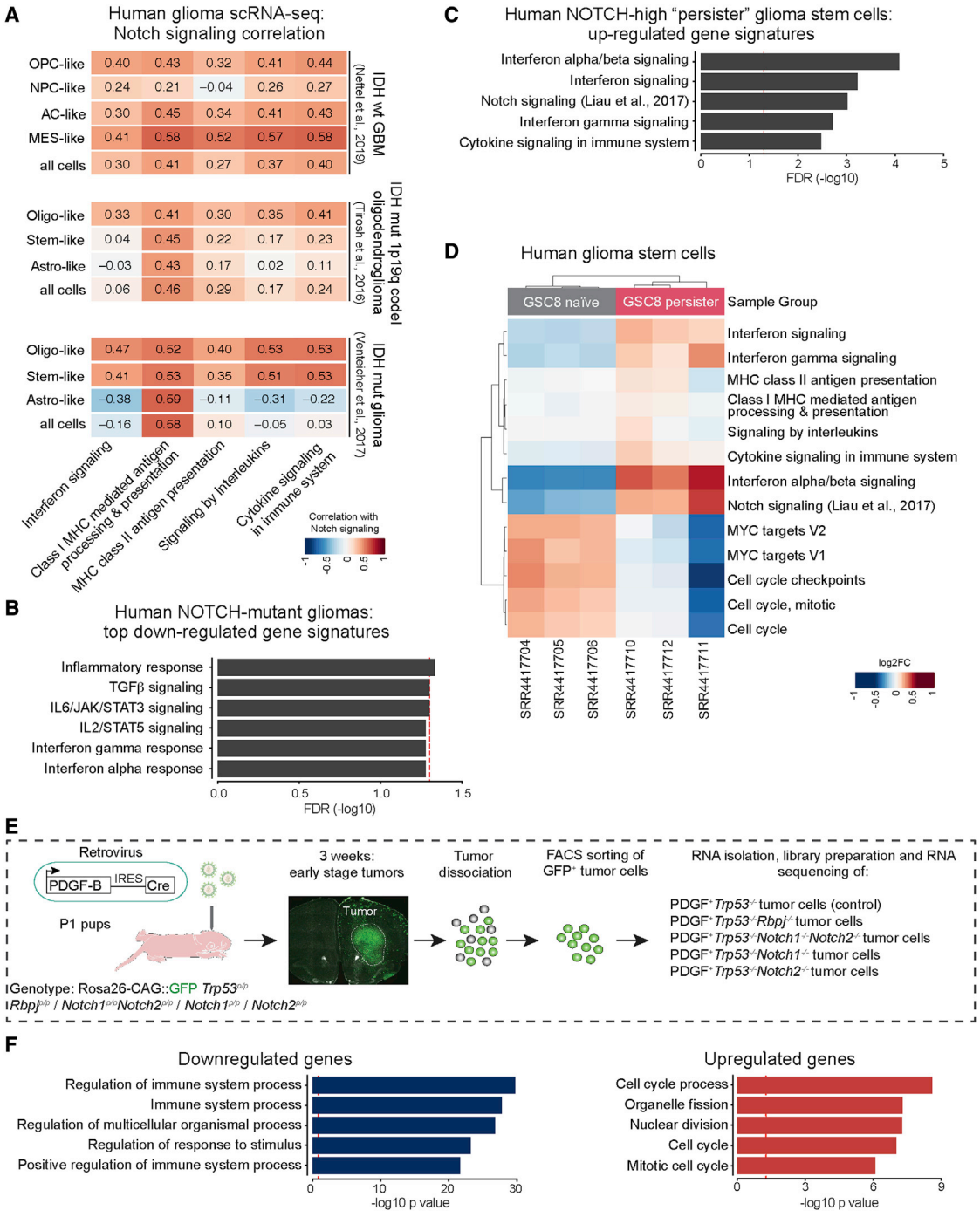

Figure 1. Expression of immune-regulatory genes and Notch activity are coordinated in human and murine gliomas

(A) Heatmap showing correlation between Notch signaling signature genes and signature genes for IFN signaling, cytokine signaling, and antigen processing and presentation in scRNA-seq datasets from multiple human glioma subtypes.

(B) GSEA showing the top downregulated gene signatures in a comparison between human IDH-mutant gliomas with and without *NOTCH1/2* inactivating mutations.

(C) GSEA of IFN signaling, cytokine signaling, and Notch signaling signature genes in the comparison between human GBM persister and naive cells.

(D) GSEA heatmap of IFN signaling, cytokine signaling, MYC signaling, cell-cycle, and Notch signaling signature genes in the comparison between human GBM persister and naive cells.

(legend continued on next page)

particularly critical in incurable brain tumors including gliomas because of their immunosuppressive nature and the unique immune microenvironment of the central nervous system.

Glioblastomas (GBMs; WHO grade 4 gliomas) are the most aggressive brain tumors and resistant to current standard and targeted therapeutic interventions (Lim et al., 2018). Immune evasion is pronounced in glioma and particularly in GBMs, which hampers immunotherapy in most patients (Cloughesy et al., 2019; Jackson et al., 2019; Schalper et al., 2019; Zhao et al., 2019). The type of glioma dictates the immune response, implying that tumor-intrinsic factors shape the composition of the TME (Friebel et al., 2020; Gangoso et al., 2021; Klemm et al., 2020; Wang et al., 2017). Leveraging TME-targeted therapies requires an understanding of the nature of these brain tumor-intrinsic factors, which is currently lacking. It is also imperative to understand whether the pro-tumorigenic immune niche observed in late-stage gliomas is already established early during gliomagenesis. The transition to a mesenchymal-like glioma cell state has been associated with increased immune infiltration and a more immunosuppressive TME (Gangoso et al., 2021; Schmitt et al., 2021; Wang et al., 2017). However, the role of the immune niche in proneural glioma, a transcriptional subtype that is considered the ancestor of all GBM subtypes, remains undefined (Gangoso et al., 2021; Ozawa et al., 2014; Schmitt et al., 2021; Wang et al., 2017). Thus, the mechanisms fostering immune escape within the glioma microenvironment are poorly understood and disguised by disease heterogeneity. A detailed mechanistic insight into the glioma cell-immune niche crosstalk could reveal new therapeutic avenues.

The Notch pathway is a fundamental niche signal that regulates stem cells across the body. In the postnatal mammalian brain, Notch promotes maintenance and quiescence of neural stem cells (NSCs) (Engler et al., 2018; Imayoshi et al., 2010; Lugert et al., 2010; Zhang et al., 2019). However, paradoxically, a consensus on the role of Notch in glioma is still lacking. Alterations in the Notch pathway have been linked with gliomagenesis, but data support both tumor-promoting and tumor-suppressing functions for Notch signaling (Jung et al., 2021; Parmigiani et al., 2020). These opposing roles of Notch are likely related to the genomic and epigenomic heterogeneity of gliomas and the multifaceted, context-dependent roles of Notch in several tissues and cancer types (Cancer Genome Atlas Research Network et al., 2015; Capper et al., 2018; Neftel et al., 2019; Nowell and Radtke, 2017; Parmigiani et al., 2020; Suzuki et al., 2015; Verhaak et al., 2010). Reduced Notch signaling is associated with worse clinical presentation and prognosis in patients with proneural, isocitrate dehydrogenase (IDH) wild-type or mutant gliomas, and inactivating mutations in Notch pathway components have been detected in IDH-mutant tumors (Aoki et al., 2018; Bai et al., 2016; Cancer Genome Atlas Research Network et al., 2015; Giachino et al., 2015; Halani et al., 2018; Somasundaram et al., 2005; Suzuki et al., 2015). The processes underlying Notch tumor-suppressive activity and pathway inhibition in human glioma subtypes remain elusive (Bai et al., 2016; Cancer Genome Atlas Research Network et al., 2015; Chow et al., 2017; Giachino et al., 2015; Halani et al., 2018; Parmigiani et al., 2020; Phillips et al., 2006; Somasundaram et al., 2005; Suzuki et al., 2015).

Combining human glioma stem cell (GSC) cultures, analyses of human glioma datasets, conditional genetics in immunocompetent preclinical models of proneural glioma, and single-cell profiling of immune cells, we demonstrate that intrinsic Notch signaling in proneural tumor cells dictates the composition of the immune niche in the TME. Attenuated Notch activity reshapes infiltration of subpopulations of myeloid and lymphoid cells into the tumor and decreases tumor responses to interferon-γ (IFNγ). Our findings indicate that reducing physiological Notch levels can be exploited by brain tumor cells to reinforce immune evasion and promote activated stem-cell-driven, niche-independent growth early during glioma formation.

RESULTS

Expression of immune-regulatory genes and Notch activity are coordinated in human and murine gliomas

We addressed whether the local immunophenotype in glioma is regulated by Notch signaling. We analyzed the expression of Notch pathway components and immune-regulatory genes in published human glioma single-cell RNA sequencing (scRNA-seq) datasets (Neftel et al., 2019; Tirosh et al., 2016; Venteicher et al., 2017). *NOTCH1*, *NOTCH2*, *RBPJ*, and *HEY1* were co-expressed with IFNγ signaling and MHC-I components in subpopulations of GBM cells, suggesting possible cross-regulation (Figure S1A). Notch signaling and gene categories related to IFN, cytokine signaling, and antigen processing and presentation had moderate positive correlation in glioma, particularly in tumor cells with oligodendrocyte progenitor cell-like features, a cellular state that is associated with the proneural transcriptional subtype (OPC-like/oligo-like cells) (Figure 1A; Neftel et al., 2019). Conversely, gene set enrichment analysis (GSEA) revealed that human IDH-mutant, lower-grade glioma samples with concomitant *NOTCH1* or *NOTCH2* mutations had low inflammatory response gene signature levels (Figure 1B; Bai et al., 2016). Notch signaling contributes to intratumoral heterogeneity in human GBM, and increased Notch activity allows transition of tumor cells to slow-cycling and drug-tolerant "persister" states in a subset of *PDGFRA*-amplified human proneural GSC lines (Charles et al., 2010; Liau et al., 2017). GSEA revealed that IFN- and cytokine-signaling gene signatures were higher in Notch-high "persister" cells compared with Notch-low "naive" cells (Figures 1C and 1D; Liau et al., 2017). Therefore, Notch pathway activity or Notch mutations can affect expression of immune-regulatory genes in human gliomas. We subdivided TCGA GBM samples into Notch-high and Notch-low using combined

(E) Scheme of glioma induction and RNA-seq profiling of tumor cells. Early tumors (3 weeks after induction) were dissociated and GFP$^+$ glioma cells purified by FACS for RNA-seq.

(F) GO term analysis (biological process) on the genes that were either significantly downregulated or upregulated (adjusted p value < 0.05, $\log_2$-fold change > 1 or < -1) in *Rbpj*$^{-/-}$ tumor cells compared with control tumor cells.

Dashed line in (B), (C), and (F) represents FDR 0.05.

See also Figure S1 and Table S1.

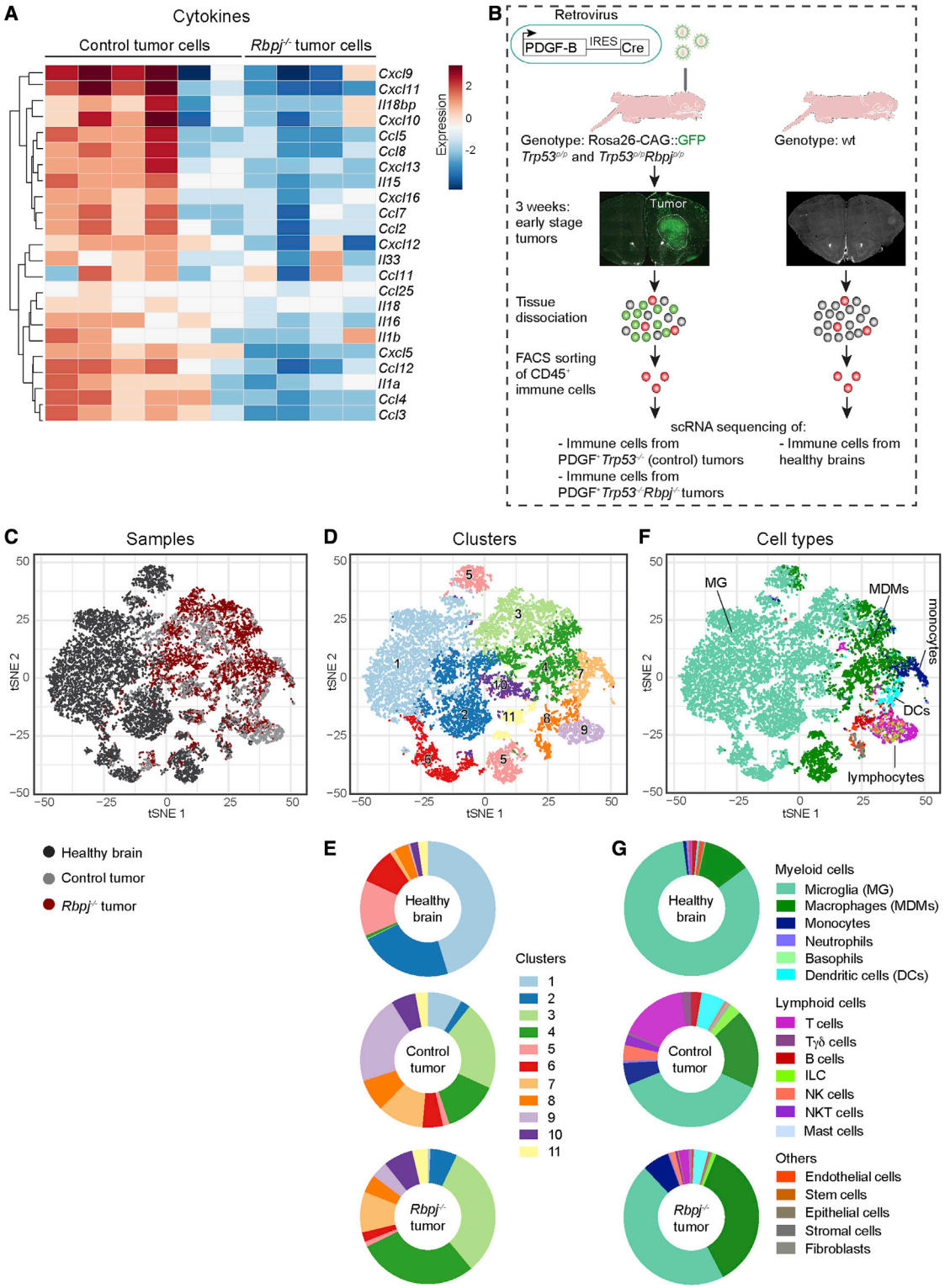

Figure 2. Reduced Notch activity in malignant cells promotes immune niche remodeling by altering the cross-talk between early tumors and the TME

(A) Expression heatmap of selected cytokine genes in 4 *Rbpj*$^{-/-}$ and 6 control glioma sample replicates. Data from RNA-seq of GFP^{+} glioma cells directly FACS-purified from tumors.

(B) Scheme of glioma induction and scRNA-seq profiling of tumor-associated immune cells and immune cells from healthy brains. Early tumors (3 weeks) and age-matched healthy brain tissue were dissociated and CD45^{+} cells purified by FACS for 10× scRNA-seq.

(legend continued on next page)

expression of canonical Notch target genes (*HEY1*, *HEY2*, and *HES5*) (Giachino et al., 2015). We used the ESTIMATE method to infer tumor-associated immune cells in Notch-high and Notch-low GBMs, focusing on major myeloid and lymphoid subpopulations observed in glioma (monocyte-derived macrophages [MDMs], tissue-resident microglia [MG], $CD4^+$ T cells, and $CD8^+$ T cells) (Bowman et al., 2016; Yoshihara et al., 2013). We found augmented MDM and reduced MG gene signatures in Notch-low relative to Notch-high GBMs, suggesting that Notch activity could control the recruitment of tumor-associated immune cells in glioma (Figure S1B).

To test this hypothesis and be able to study co-evolution of tumor cells and their immune niche *in vivo*, we utilized a mouse model of human glioma. We simulated alterations commonly found in proneural GBM, including elevated PDGF signaling in combination with mutation of the tumor suppressor p53, by retrovirus-mediated expression of PDGF and Cre-recombinase (Cre) deletion of floxed *Trp53* alleles in mice (Giachino et al., 2015; Verhaak et al., 2010). Tumor cells were genetically labeled with GFP following recombination of a Cre-reporter allele (*Rosa-CAG::GFP*), discriminating them from the TME *in vivo* (Figure 1E). We blocked Notch signaling components by conditional genetics specifically in the tumor cells, thereby recapitulating Notch signal inhibition that occurs in several cancers and in some forms of human proneural glioma (Bai et al., 2016; Cancer Genome Atlas Research Network et al., 2015; Giachino et al., 2015; Nowell and Radtke, 2017; Suzuki et al., 2015). We transcriptionally profiled $PDGF^+Trp53^{-/-}$ glioma cells with intact Notch signaling (hereafter referred to as control tumors) and $PDGF^+Trp53^{-/-}$ glioma cells lacking the key Notch mediator *Rbpj*, *Notch1*, *Notch2*, or *Notch1* and *Notch2* (hereafter referred to as $Rbpj^{-/-}$, $Notch1^{-/-}$, $Notch2^{-/-}$, and $Notch1^{-/-}Notch2^{-/-}$ tumors) (Figure 1E). We focused on the initial cell-autonomous changes resulting from Notch inhibition by isolating the GFP^+ cancer cells by fluorescence-activated cell sorting (FACS) at an early stage of tumor formation, 3 weeks after glioma induction (Figure 1E). We confirmed deletion of Notch alleles and loss of proteins by genotyping and western blotting (Figures S1C and S1D). RNA-seq revealed many differentially expressed genes between control and $Rbpj^{-/-}$, $Notch1^{-/-}Notch2^{-/-}$, and $Notch1^{-/-}$ tumor cells, and more moderate changes following deletion of *Notch2* ($Notch2^{-/-}$) (Figure S1E). Gene ontology (GO) analysis revealed a decrease in the expression of immune-regulatory genes in all Notch-knockout tumor genotypes and, conversely, an increase in the expression of genes associated with cell proliferation in $Rbpj^{-/-}$, $Notch1^{-/-}Notch2^{-/-}$, and $Notch1^{-/-}$, but not $Notch2^{-/-}$ cells (Figure 1F; Table S1). We ranked glioma genotypes from those with the least to the most aggressive clinical presentation (control tumor < $Notch2^{-/-}$ < $Notch1^{-/-}$ < $Notch1^{-/-}Notch2^{-/-}$ ≈ $Rbpj^{-/-}$) based on survival data (Giachino et al., 2015; Figure S1F). To identify gene signatures that correlated with glioma aggressiveness, we grouped genes based on changes in their expressions ("switches") that characterized the transitions toward increased malignancy across the different Notch mutant tumors (Figure S1G). We observed reduced expression of proliferative quiescence-associated genes (*Id4*, *Vcam1*) and increased expression of oncogenes (*Myc*, *Fos*, *Atf5*) over control tumors in $Rbpj^{-/-}$, $Notch1^{-/-}Notch2^{-/-}$, and $Notch1^{-/-}$ but not in $Notch2^{-/-}$ tumors. However, the expression of several immune-regulatory genes was consistently reduced in all Notch-knockout tumors ($Rbpj^{-/-}$, $Notch1^{-/-}Notch2^{-/-}$, $Notch1^{-/-}$, $Notch2^{-/-}$) compared with control tumors (Figure S1G; Table S1). These data implied that Notch-mediated immune niche remodeling plays a major role in the aggressiveness of proneural glioma shortly after tumor initiation.

Reduced Notch activity in malignant cells promotes immune niche remodeling by altering the cross-talk between early tumors and the TME

The majority of the genes differentially expressed between Notch-knockout and control tumor cells were associated with immune-regulatory functions (Figure 1F; Table S1). Multiple cytokines involved in the recruitment and activation of both myeloid and lymphoid cells were downregulated in all Notch-knockout tumor genotypes (Figures 2A and S2A). This suggested that deletion of Notch signaling components has an impact on the communication between tumor cells and the immune system. In order to address immune cell composition within early tumors, we performed scRNA-seq on $CD45^+$ immune cells from $Rbpj^{-/-}$ gliomas, control gliomas, and healthy brain tissue (Figures 2B and S2B). Unsupervised hierarchical clustering revealed eleven immune cell clusters with distinct gene signatures (Figures 2C and 2D). Some of these clusters were more prevalent in healthy brains (clusters 1, 2, 5, and 6), and others were overrepresented in the glioma microenvironment (clusters 3, 4, 7, 9, and 10) (Figure 2E; Table S2). Moreover, the contribution of some immune cell clusters to the TME was either reduced (clusters 1, 6, and 9) or increased (clusters 3, 4, and 10) in $Rbpj^{-/-}$ tumors compared with control tumors (Figure 2E). Analysis of the genes defining immune cell subsets suggested a decrease in MG and an increase in MDMs and lymphocytes in the TME compared with the healthy brain (Figures 2F, 2G, and S2C). However, although T cells dominated the lymphoid compartment in control tumors, they were reduced in $Rbpj^{-/-}$ gliomas where MDMs and macrophage-like populations were increased (Figure 2G). Thus, loss of *Rbpj* and Notch signaling in tumor cells profoundly modified the immune TME already at an early stage (3 weeks) of glioma development. These findings reinforce our observation of a link between Notch, inflammatory responses, and glioma immunophenotype in humans (Figures 1 and S1).

(C) t-distributed stochastic neighbor embedding (t-SNE) visualization of $CD45^+$ cells sorted from healthy brains, $Rbpj^{-/-}$ gliomas, and control gliomas.
(D) t-SNE projection of clusters of $CD45^+$ cells from healthy brains, $Rbpj^{-/-}$ gliomas, and control gliomas.
(E) Distribution of immune cells in clusters of $CD45^+$ cells across healthy brains, $Rbpj^{-/-}$ tumors, and control tumors.
(F) Immune cell type allocation (proposed by nearest-neighbors classification with SingleR) on a t-SNE plot of $CD45^+$ cells from healthy brains, $Rbpj^{-/-}$ gliomas, and control gliomas.
(G) Distribution of immune cell types across healthy brains, $Rbpj^{-/-}$ tumors, and control tumors.
See also Figure S2 and Table S2.

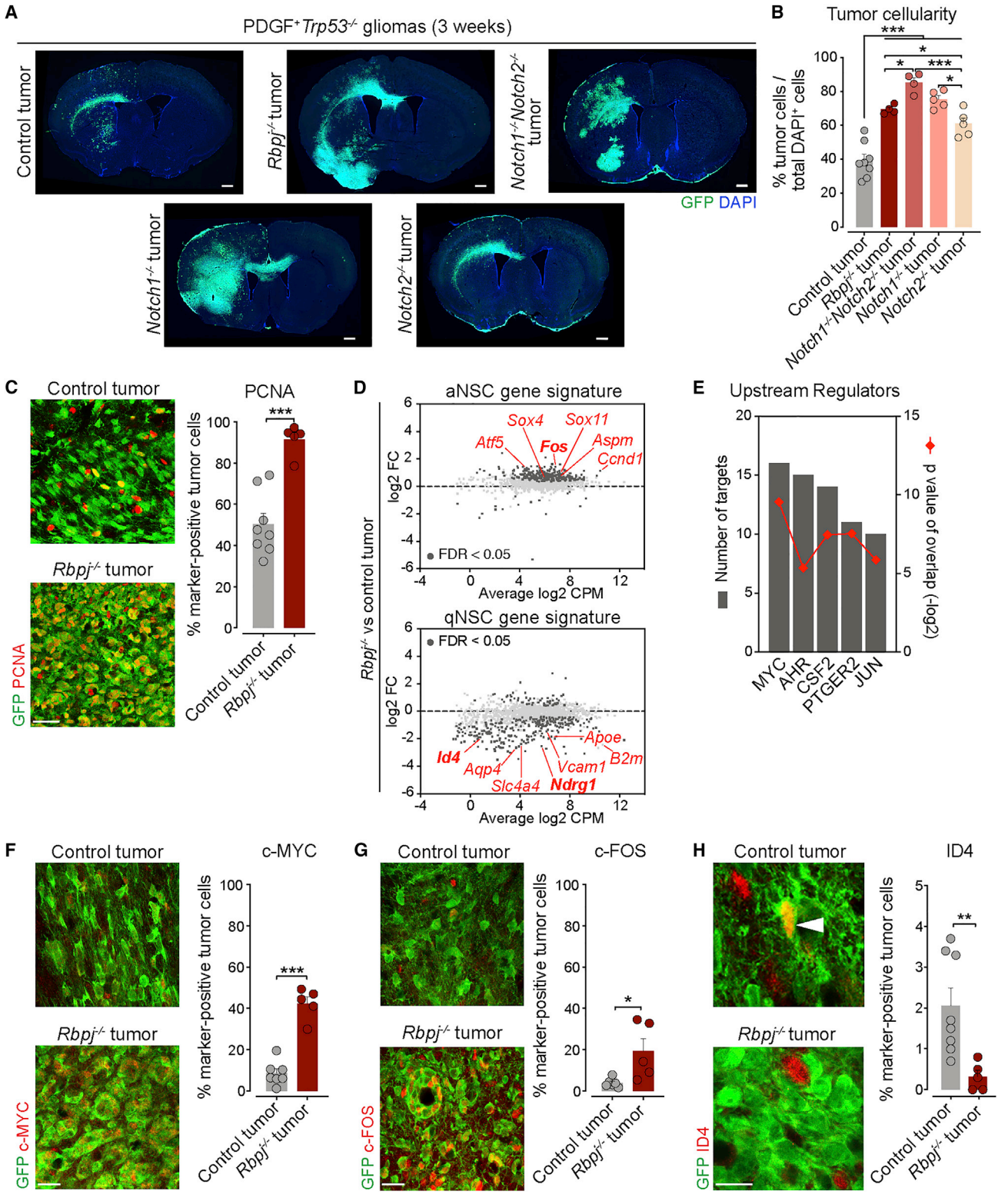

Figure 3. Inhibition of Notch signaling induces an activated stem cell trait and releases oncogene expression by tumor cells in their *in vivo* niche

(A) Images of control tumors (Notch-intact) and tumors with four different Notch-knockout genotypes (*Rbpj*$^{-/-}$, *Notch1*$^{-/-}$*Notch2*$^{-/-}$, *Notch1*$^{-/-}$, and *Notch2*$^{-/-}$) 3 weeks after glioma induction. Tumor cells are GFP^{+}.

(B) Quantification of tumor cellularity in the core of Notch-knockout and control gliomas (n = 4–8 mice).

(legend continued on next page)

Inhibition of Notch signaling induces an activated stem cell trait and releases oncogene expression by tumor cells in their *in vivo* niche

We addressed whether the altered immune TME composition after Notch inhibition coincided with differential growth of the tumors within their niche. Deletion of *Notch1* or *Notch2*, or simultaneous *Notch1* and *Notch2* deletion, promoted glioma growth similar to complete ablation of canonical Notch signaling (*Rbpj*$^{-/-}$) (Figures 3A and 3B). In addition, early-stage *Rbpj*$^{-/-}$, *Notch1*$^{-/-}$*Notch2*$^{-/-}$, and *Notch1*$^{-/-}$ gliomas contained more mitotically active cells (PCNA^{+}) than *Notch2*$^{-/-}$ and control tumors (Figures 3C and S3A). Given the central role of Notch signaling in promoting stem cell quiescence in the brain, we analyzed the expression of genes associated with mitotically quiescent NSCs (qNSCs) or with activated, dividing NSCs (aNSCs, activated NSCs) (Codega et al., 2014). We observed decreased expression of qNSC signature genes (including *Id4* and *Ndrg1*) and increased expression of aNSC signature genes (including the oncogene *Fos*) in *Rbpj*$^{-/-}$, *Notch1*$^{-/-}$*Notch2*$^{-/-}$, and *Notch1*$^{-/-}$ glioma cells compared with control glioma cells *in vivo*, but not in *Notch2*$^{-/-}$ glioma cells (Figures 3D and S3B–S3D). Ingenuity pathway analysis (IPA) identified c-MYC signaling as a regulator of the genes associated with activation of cell proliferation (Figure 3E; Table S3). We confirmed an increase in c-MYC protein by immunofluorescence of *Rbpj*$^{-/-}$, *Notch1*$^{-/-}$*Notch2*$^{-/-}$, and *Notch1*$^{-/-}$ tumors compared with *Notch2*$^{-/-}$ and control tumors (Figures 3F and S3E). Increased c-MYC positively correlated with the aNSCs marker c-FOS and inversely correlated with the qNSC marker ID4 (Figures 3G, 3H, S3F, and S3G) (Codega et al., 2014; Zhang et al., 2019). Thus, Notch inhibition boosts the growth of tumor cells within their niche, and inhibition of *Rbpj* or *Notch1* induces an activated stem cell trait in glioma cells, supporting observations in human proneural GBM (Figure 1D; Giachino et al., 2015; Liau et al., 2017).

Tumor cells promote an immunosuppressive phenotype of TAMs and acquire resistance to CSF-1R inhibition by reducing Notch activity

Due to the prominence of tumor-associated MG/macrophages (TAMs) in the TME of gliomas and their potential therapeutic relevance (Friebel et al., 2020; Klemm et al., 2020; Quail et al., 2016), we studied this population in more detail. *Rbpj*$^{-/-}$ and control tumors showed sizeable transcriptional differences in the MG/MDM population (Figure 4A). This was reflected by differences in the abundance of MDM-enriched cluster 4 and MG/MDM cluster 3, which were nearly absent from the healthy brain but were increased in the tumors and more abundant in *Rbpj*$^{-/-}$ tumors compared with control tumors (Figures 2D, 2E, and 4B). Conversely, clusters 1 and 6 cells (homeostatic MG) were predominant in the healthy brain and present in control tumors but were underrepresented in *Rbpj*$^{-/-}$ tumors (Figures 2D, 2E, and 4B). Myeloid cell clusters 3 and 4 (most highly enriched in the TME of *Rbpj*$^{-/-}$ tumors) had higher levels of immunosuppressive gene signatures than clusters 1 and 6 (Figure 4C). Comparison of MG-containing clusters 3 (enriched in *Rbpj*$^{-/-}$ tumors) and 1 (more present within healthy brains and control tumors) showed cluster 3 cells to have a more immunosuppressive profile and cluster 1 cells a more homeostatic profile (Figure 4C). Thus, Notch inhibition in tumor cells favored immunosuppressive MG/MDM populations in the TME at the expense of homeostatic MG.

The majority of the IBA1^{+} cells expressed the homeostatic MG marker TMEM119 in both healthy brains and early tumors (Figure 4D; Klemm et al., 2020). However, MG density was significantly lower in *Rbpj*$^{-/-}$ compared with control gliomas (Figure 4D). Moreover, IBA1^{+} cells were less proliferative in the TME of *Rbpj*$^{-/-}$ tumors compared with control tumors, suggesting reduced MG expansion as a consequence of Notch inhibition in the tumor cells (Figure 4E). FACS analyses confirmed a decreased contribution of CD45^{low} putative homeostatic MG to the CD11b^{+} TAM population in *Rbpj*$^{-/-}$ gliomas (Figure 4F) and a reciprocal increase in CD49d^{+} invading MDMs and peripheral monocytes (Figures 4G and S4A; Bowman et al., 2016). Upregulation of CD68 (Figure S4B) and downregulation of MHC-II (Figure S4C) by IBA1^{+} cells in *Rbpj*$^{-/-}$ tumors further supported phenotypic and functional differences between the TAM populations in control and *Rbpj*$^{-/-}$ gliomas. Together, these data indicated an accelerated pro-tumorigenic conversion of TAMs in the TME of gliomas lacking Notch signaling as compared to tumors with active Notch.

We addressed the effects of glioma cells on resident MG by co-culturing MG from healthy brains with *Rbpj*$^{-/-}$ or control GSC lines (Figures S4D–S4G). *Rbpj*$^{-/-}$ GSCs were less effective than control GSCs at promoting chemotaxis of MG in transwell assays (Figure S4D). This was in line with the reduced density of MG in *Rbpj*$^{-/-}$ tumors *in vivo* (Figure 4D). Additionally, *Rbpj*$^{-/-}$ GSCs were phagocytosed by MG less than control GSCs *in vitro* (Figure S4E). Media conditioned by control but not *Rbpj*$^{-/-}$ GSCs induced morphological and molecular changes in the MG suggestive of a pro-inflammatory activation (Figures S4F and S4G). These data indicate an altered cross-talk between tumor cells and MG/TAM populations after inhibition of Notch signaling specifically in the tumor cells, supporting our observations in human GBM (Figure S1B).

In preclinical mouse models of GBM, pro-tumorigenic "education" of TAMs can be reverted via inhibition of colony-stimulating

(C) Images of PCNA expression in *Rbpj*$^{-/-}$ and control tumors, and quantification (n = 5–8 mice).
(D) MA plots showing relative expression of activated neural stem cell (aNSC) and quiescent neural stem cell (qNSC) signature genes in *Rbpj*$^{-/-}$ versus control gliomas. Dark gray dots represent significantly differentially expressed genes (FDR < 0.05).
(E) IPA analysis of upstream regulators of the genes that were significantly upregulated in *Rbpj*$^{-/-}$ tumor cells compared with control tumor cells. The number of target genes for each pathway and the p value of overlap are shown.
(F) Images of c-MYC protein expression in *Rbpj*$^{-/-}$ and control tumors, and quantification (n = 5–7 mice).
(G) Images of c-FOS expression in *Rbpj*$^{-/-}$ and control tumors, and quantification (n = 5–6 mice).
(H) Images of ID4 expression in *Rbpj*$^{-/-}$ and control tumors, and quantification (n = 5–8 mice). An ID4^{+} tumor cell (GFP^{+}) is indicated by the arrowhead.
Data represent mean ±SEM. *p < 0.05, **p < 0.01, ***p < 0.001. One-way ANOVA with Tukey's multiple comparisons test (B), Student's t test (C and F–H). Scale bars: 500 μm in (A) and 20 μm in (C) and (F)–(H).
See also Figure S3 and Table S3.

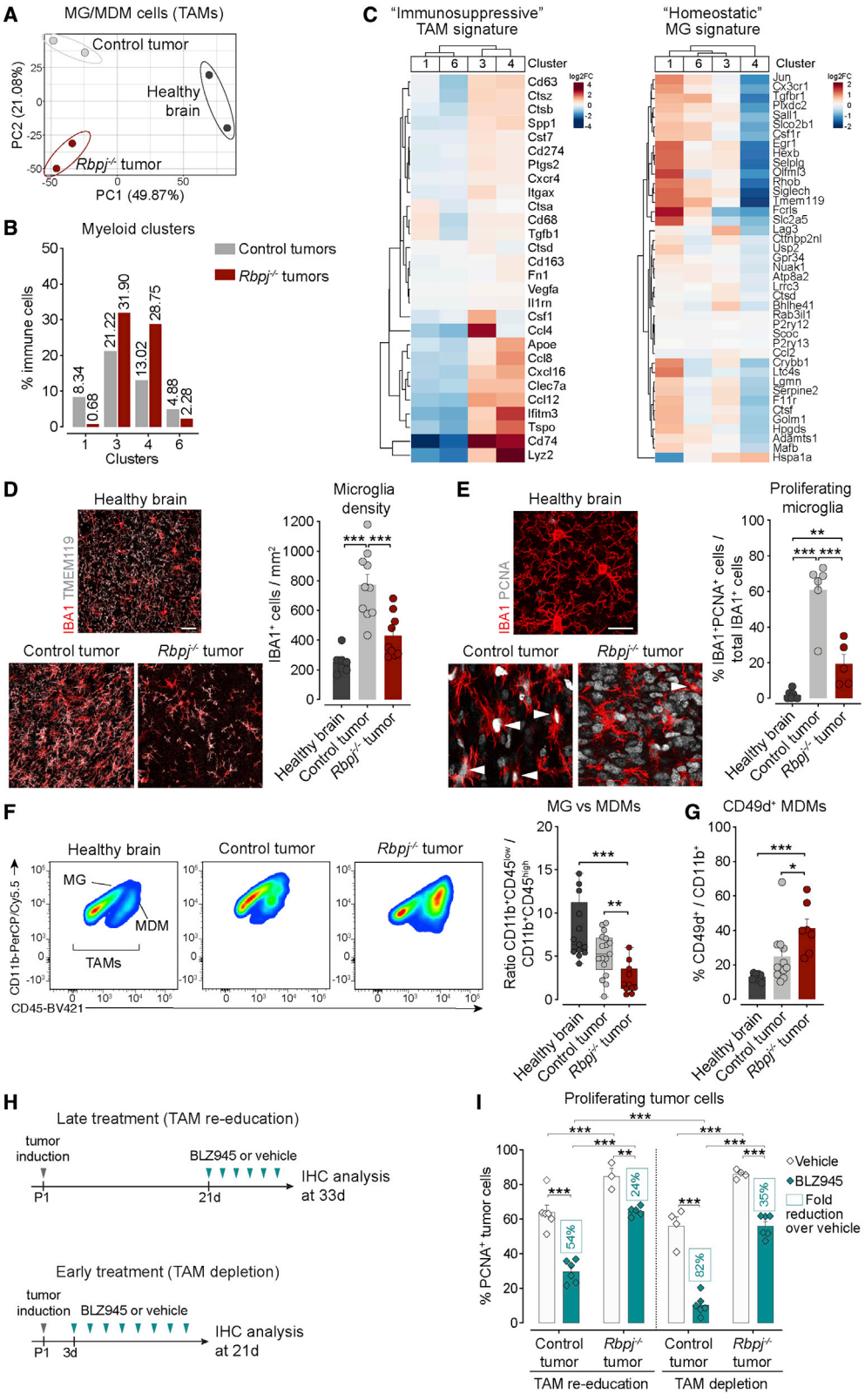

(legend on next page)

factor-1 receptor (CSF-1R) (Quail et al., 2016). We addressed whether Notch-deficiency interferes with blocking CSF-1R by challenging PDGF^{+}*Trp53*$^{-/-}$ tumors with an early and late treatment strategy with the CSF-1R inhibitor BLZ945 (Figures 4H and S4H) (Pyonteck et al., 2013). The early treatment regime depletes MG and MDMs prior to tumor formation and the late treatment regime "re-educates" TAMs to an anti-tumorigenic phenotype within the TME. Both early and late inhibition of CSF-1R reduced dividing (PCNA^{+}) control tumor cells and the expression of OLIG2, a transcription factor involved in glioma proliferation (Figures 4I and S4I) (Mehta et al., 2011). Thus, TAMs are tumor-promoting early after glioma initiation and not only during glioma progression. In contrast, BLZ945 treatment was significantly less effective at reducing proliferation and OLIG2 expression of *Rbpj*$^{-/-}$ tumor cells (Figures 4I and S4I). This difference was particularly striking following the early depletion protocol, which resulted in a 4-fold (approximately 80%) reduction in PCNA and OLIG2 expression in Notch-intact control tumors, compared with only 35% reduction in PCNA and no significant change in OLIG2 expression in *Rbpj*$^{-/-}$ tumor cells (Figures 4I and S4I). Therefore, *Rbpj*$^{-/-}$ gliomas can overcome the absence of pro-tumorigenic TAMs in the TME suggesting that reduced Notch signaling could contribute to resistance to CSF-1R inhibition.

Tumors alter their T cell content by reducing Notch activity

GBMs establish an immunosuppressive TME that leads to T cell dysfunction (Jackson et al., 2019). Depletion of T cell subsets positively correlates with a worse overall survival of patients with IDH wild-type gliomas (Friebel et al., 2020). *Rbpj*$^{-/-}$ glioma cells have reduced expression of chemokines and interleukins involved in T cell migration and activation, including CXCL9, CXCL10, IL-15, and IL-16 (Figure 2A) and a lower number of T cells in the TME (Figure 2G). These changes suggest that loss of Notch activity in malignant cells may contribute to impaired T cell recruitment at early stages of tumor formation. RNA-seq analysis of tumor cells revealed downregulation of several components of the antigen processing and presentation machinery in all Notch-knockout tumor genotypes compared with control tumors and a reduction in the expression of the key regulators of MHC expression *Nlrc5* and *Ciita* (Figures 5A and S5A; Kobayashi and van den Elsen, 2012). We confirmed these reductions in expression by qPCR of transcripts from acutely sorted *Rbpj*$^{-/-}$ and control glioma cells (Figure 5B). Flow cytometry confirmed a reduced contribution of T lymphocytes to the TME of *Rbpj*$^{-/-}$ tumors and a decreased T cell/tumor cell ratio implying a compromised immune surveillance (Figures 5C and S5B). Low T cell numbers in *Rbpj*$^{-/-}$ tumors correlated with a reduced number of dendritic cells that are critical for cytotoxic T lymphocyte priming (Figure 2G; Hildner et al., 2008; Tussiwand et al., 2012). *Rbpj*$^{-/-}$ gliomas showed a specific reduction in the density of CD8^{+} T cells, whereas CD4^{+} T cell and NKp46^{+} natural killer (NK) cell densities were comparable with that in control tumors (Figures 5D, S5C, and S5D). GSEA of the T cell scRNA-seq data indicated increased proliferation and activation of T cells in both *Rbpj*$^{-/-}$ and control tumors compared with healthy brain tissue (Figures 5E, S5E, and S5F; Table S4). However, Notch-depleted tumors had lower numbers of T cells expressing markers of activation (CD69) and effector functions (Perforin, Granzyme), as well as co-stimulatory molecules (ICOS) and co-inhibitory receptors (PD1, TIM-3, CTLA4) compared with control tumors (Figures 5F and S5G). Thus, inhibition of Notch signaling in tumor cells resulted in differences in T cell numbers in the TME already at an early stage of the disease.

To address whether the presence of T cells affects early stages of glioma formation and to partially simulate the effects of Notch-deletion on the T cell compartment, we eliminated all T cells prior to tumor development by chronic antibody-mediated T cell depletion *in vivo* (Figures 5G, S5H, and S5I). 3 weeks after tumor induction, the proportion of dividing (PCNA^{+}) tumor cells increased significantly in the absence of T cells in control gliomas, but not in *Rbpj*$^{-/-}$ tumors (Figure 5H). Thus, T lymphocytes played a Notch signal-dependent, tumor-suppressive role during early growth of PDGF^{+}*Trp53*$^{-/-}$ gliomas. These data suggested that reduced T cell levels in Notch-depleted tumors could facilitate immune evasion and promote tumor growth.

Figure 4. Tumor cells promote an immunosuppressive phenotype of TAMs and acquire resistance to CSF-1R inhibition by reducing Notch activity

(A) Principal-component analysis (PCA) comparing the *in silico*-bulk expression profiles of the MG/MDM population (TAMs) of healthy brains, *Rbpj*$^{-/-}$ tumors, and control tumors, using the top 25% of the most variable genes. We generated *in silico*-bulk myeloid expression profiles for each tissue-type in duplicate (two healthy brain, two control tumor, and two *Rbpj*$^{-/-}$ tumor sample replicates) by pooling single MG/MDM cells in each sample. Duplicate sample replicates of each tissue are shown.

(B) Percentages of immune cells in myeloid cell clusters 1, 3, 4, and 6 in *Rbpj*$^{-/-}$ and control tumors.

(C) Gene expression heatmaps of signature genes of immunosuppressive TAMs and homeostatic MG in myeloid-cell-containing clusters 1, 3, 4, and 6.

(D) Images of IBA1^{+}/TMEM119^{+} MG cells in healthy brains, and in the core of *Rbpj*$^{-/-}$ and control tumors, and quantification of IBA1^{+} cell density (n = 7–10 mice).

(E) Images of proliferating (PCNA^{+}) IBA1^{+} cells in healthy brains, and in the core of *Rbpj*$^{-/-}$ and control tumors, and quantification of the proportion of IBA1^{+} cells expressing PCNA (n = 5–7 mice). PCNA^{+}IBA1^{+} cells are indicated by arrowheads.

(F) Flow cytometry analysis of CD11b^{+}CD45^{low} MG and CD11b^{+}CD45^{high} MDM cells, and ratios of MG/MDM cells in healthy brains, *Rbpj*$^{-/-}$ tumors, and control tumors (n = 11–17 mice).

(G) Flow cytometry analysis showing the percentage of CD49d^{+} MDM cells among the CD11b^{+} population in healthy brains, *Rbpj*$^{-/-}$ tumors, and control tumors (n = 7–11 mice).

(H) Scheme of experimental design for late (TAM "re-education") and early (TAM depletion) CSF-1R inhibitor (BLZ945) treatment schedules.

(I) Quantification of glioma cell proliferation (PCNA immunostaining) in *Rbpj*$^{-/-}$ tumors and control tumors after late BLZ945, early BLZ945, or vehicle treatment (n = 3–6 mice).

Data represent mean ± SEM. *p < 0.05, **p < 0.01, ***p < 0.001. One-way ANOVA with Tukey's multiple comparisons test (D–G), two-way ANOVA with Šídák's (between genotypes) or Tukey's (between treatments) multiple comparisons test (I). Scale bars: 30 μm in (D) and 20 μm in (E).

See also Figure S4.

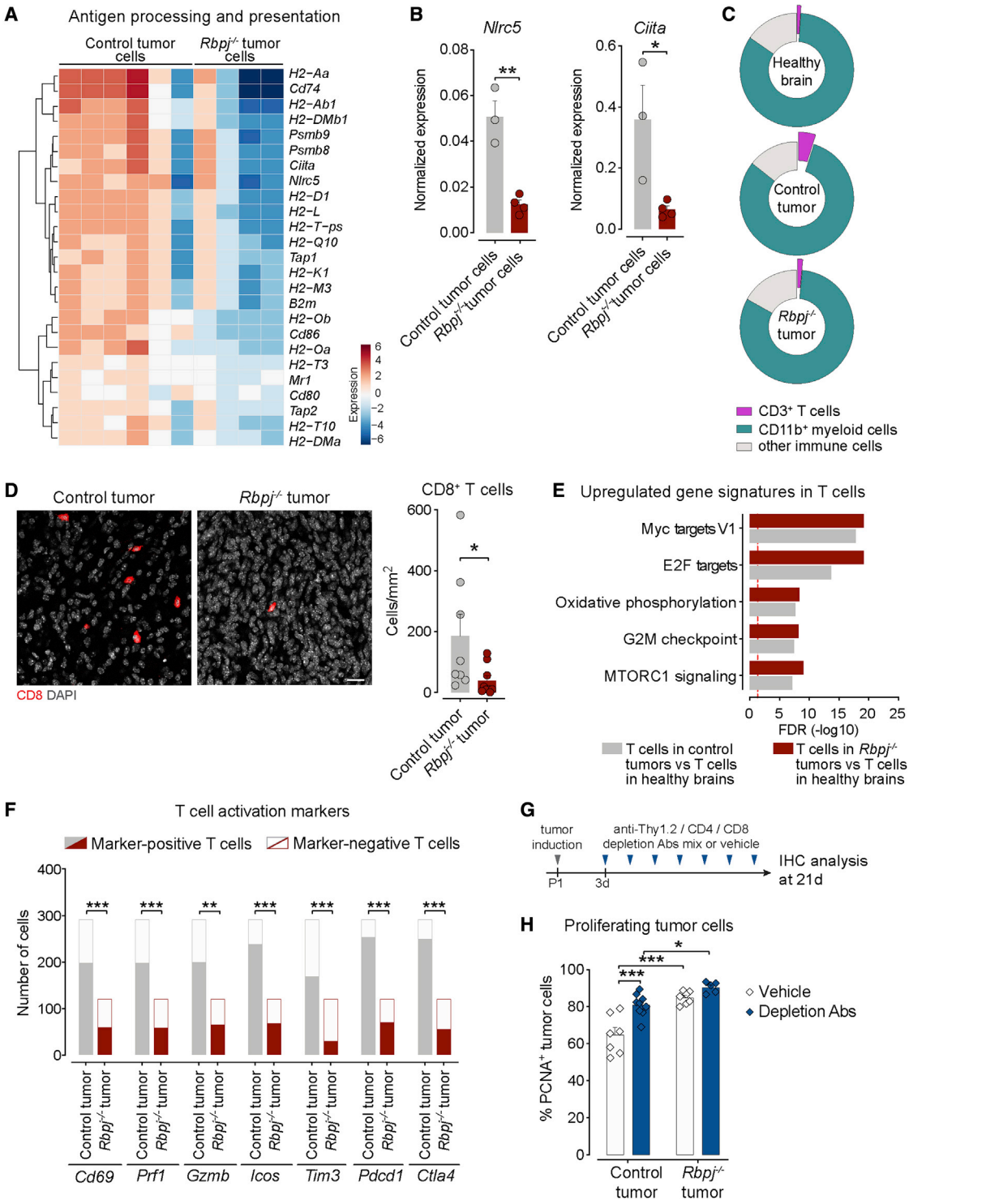

Figure 5. Tumors alter their T cell content by reducing Notch activity

(A) Heatmap of expression of genes involved in antigen processing and presentation in 4 *Rbpj*$^{-/-}$ and 6 control glioma sample replicates. Data from RNA-seq of GFP^{+} glioma cells directly FACS-purified from tumors.

(B) Quantification of *Nlrc5* and *Ciita* expression (qPCR) by *Rbpj*$^{-/-}$ and control glioma cells directly FACS-purified from tumors (n = 3–4 mice).

(C) Contribution of CD3^{+} T cells to the CD45^{+} immune cell population in healthy brains, *Rbpj*$^{-/-}$ tumors, and control tumors (flow cytometric analysis).

(D) Images of CD8 immunostaining and quantification in the core of *Rbpj*$^{-/-}$ and control tumors (n = 8–9 mice).

(E) GSEA of T cells from *Rbpj*$^{-/-}$ and control tumors compared with T cells from healthy brains. The top upregulated gene categories are shown. Dashed line represents FDR 0.05.

(legend continued on next page)

Notch regulates interferon-γ response of human and murine tumor cells

To uncover pathways that orchestrate immune niche remodeling, we performed IPA analysis and determined the regulators of the genes that were decreased in tumor cells as a result of Notch inhibition. IFNγ signaling was a prominent putative upstream regulator (Figures 6A and S6A; Table S5). GSEA of RNA-seq data and qPCR analysis indicated that multiple components of the IFNγ pathway were downregulated in multiple Notch-knockout glioma types (Figures 6B, S6B, and S6C). To determine the IFNγ response of the tumor cells, we treated multiple *Rbpj*$^{-/-}$ and control GSC lines with IFNγ *in vitro*. Increasing IFNγ concentrations induced cell death and inhibited proliferation of control GSC lines, but *Rbpj*$^{-/-}$ cells were more refractory to the treatment (Figures 6C and 6D). These results suggested that the IFNγ signaling pathway was constitutively blunted in tumor cells lacking *Rbpj* and Notch signaling and were in line with our analyses of human glioma datasets (Figures 1A–1D).

We analyzed the IFNγ response of *Rbpj*$^{-/-}$ and control GSC lines at the molecular level. Expression of IFNγ receptor was similar in *Rbpj*$^{-/-}$ and control GSCs (Figure S6D). However, *Rbpj*$^{-/-}$ GSCs had a significant reduction in STAT1 and STAT3 phosphorylation upon IFNγ treatment compared with control GSCs (Figure 6E). Although IFNγ stimulation efficiently induced transcription of the IFNγ target genes and effectors IRF5 and IRF7 by control GSCs, IFNγ treatment did not increase IRF5 and IRF7 expression as effectively by *Rbpj*$^{-/-}$ GSCs (Figure 6F). In contrast, IRF1 transcription was induced similarly by IFNγ in control and *Rbpj*$^{-/-}$ GSC lines (Figure S6E). In support of a reduced IFNγ response, *Rbpj*$^{-/-}$ and Notch receptor knockout tumors showed reduced expression of IRFs *in vivo* (Figures 6B, S6B, and S6C). We addressed whether Notch inhibition interferes with IFNγ response in human GSCs. We established GSC tumorsphere cultures of two independent IDH1-wild-type, PDGFRA-amplified GBM cell lines of the proneural subtype (GSC8 and GSC125) (Liau et al., 2017) and treated these with IFNγ in combination with the gamma secretase/Notch inhibitor DAPT. DAPT did not affect IFNγ receptor levels but significantly reduced STAT1 phosphorylation upon IFNγ treatment in GSC8 and GSC125 cells (Figures 6G and S6F). Thus, Notch activity regulates IFNγ signaling in human and murine proneural glioma cells.

Blunted IFNγ response in tumor cells with reduced Notch activity promotes immune evasion

Several Notch-regulated IFNγ signaling molecules are involved in the chemoattraction and function of the adaptive and innate immune system (Figures 2A, 5A, and S6A). We speculated that a reduced IFNγ response in Notch-knockout gliomas could curtail the recruitment of IFNγ-producing immune cell populations into the TME, thereby establishing a non-cell-autonomous inhibitory feedback loop that amplifies immune evasion by the tumors. Our scRNA-seq data indicated that *Ifng*-expressing immune cells were reduced in the TME of *Rbpj*$^{-/-}$ tumors (Figure 7A). Moreover, CD45^{+} cells expressing the IFNγ-regulating transcription factor *Tbx21* (T-bet) were reduced in *Rbpj*$^{-/-}$ compared with control tumors (Figure 7A). T cells and NK cells are the major IFNγ-producing immune cell types and mediate cancer immune surveillance (Barrow et al., 2018; Binnewies et al., 2018). We observed that CD8^{+} T cells, but not CD4^{+} T cells or NK cells, were decreased in *Rbpj*$^{-/-}$ gliomas compared with control tumors (Figures 5D, S5C, and S5D). In addition, *Ifng*-expressing immune cells predominantly grouped within cluster 9 (Figure 7A), which was mainly composed of CD8^{+} T lymphocytes (Figure S7A). The abundance of *Ifng*- or *Tbx21*-expressing T cells was reduced in the TME of *Rbpj*$^{-/-}$ gliomas compared with control tumors (Figures 7B, S7B, and S7C). In contrast, other *Ifng*- or *Tbx21*-expressing immune cell populations, including TAMs, were infrequent, and their abundance did not change in *Rbpj*$^{-/-}$ tumors (Figures S7B and S7D).

Finally, we assessed IFNγ-dependent cytokine and MHC-I expression in GSC tumorsphere cultures. Exposure of control GSCs to IFNγ induced transcription of cytokines that stimulate myeloid (*Ccl2*, *Ccl5*) and lymphoid (*Il15*) cell recruitment (Figure 7C). Conversely, *Ccl2*, *Ccl5*, and *Il15* induction was significantly impaired in *Rbpj*$^{-/-}$ GSC lines, even after extended exposure to IFNγ (Figure 7C). IFNγ treatment of control GSCs also rapidly induced expression of the MHC-I transactivator *Nlrc5* and cell surface expression of MHC-I molecules, including both heavy α-chain and β-2-microglobulin (B2M) (Figures 7D, 7E, and S7E). In contrast, the induction of the MHC-I components was dramatically compromised in *Rbpj*$^{-/-}$ GSCs (Figures 7D, 7E, and S7E). These data indicate that Notch-knockout gliomas have a blunted MHC-I and cytokine production downstream of IFNγ stimulation, exacerbated by lower recruitment of IFNγ-expressing immune cell populations.

DISCUSSION

Cancer cells are faced with two major challenges for their growth and survival: to proliferate avoiding the normal mitotic restriction mechanisms and to elude niche control escaping elimination by the immune system. Often, these events necessitate accumulation of different genetic and epigenetic alterations. Here, we show that the levels of Notch signaling contribute to both cell-autonomous regulation of cell proliferation and tumor-cell immune resistance at multiple levels. Reducing physiological Notch activity can be exploited by glioma cells to attenuate IFNγ response, promote the development of an immunosuppressive TME, reinforce immune evasion, and boost activated stem-cell-driven, immune niche-independent proliferation (Figure 7F). Thus, our data provide insights into how the

(F) Quantification of T lymphocytes expressing markers of activation (*Cd69*), effector function (*Gzmb*, *Prf1*), co-stimulatory (*Icos*), or co-inhibitory (*Pdcd1*, *Tim3*, *Ctla4*) molecules in *Rbpj*$^{-/-}$ and control tumors. Data are extracted from scRNA-seq analysis of CD45^{+} cells.
(G) Scheme of experimental design for antibody-mediated early T cell depletion in *Rbpj*$^{-/-}$ and control tumor-bearing mice.
(H) Quantification of cell proliferation (PCNA^{+} cells) in *Rbpj*$^{-/-}$ and control tumors after treatment with T cell depletion antibodies or vehicle (PBS) (n = 5–9 mice).
Data represent mean ± SEM. *p < 0.05, **p < 0.01, ***p < 0.001. Student's t test (B and D), Fisher's exact test (F), two-way ANOVA with Šídák's multiple comparisons test (H). Scale bars, 20 μm (D).
See also Figure S5 and Table S4.

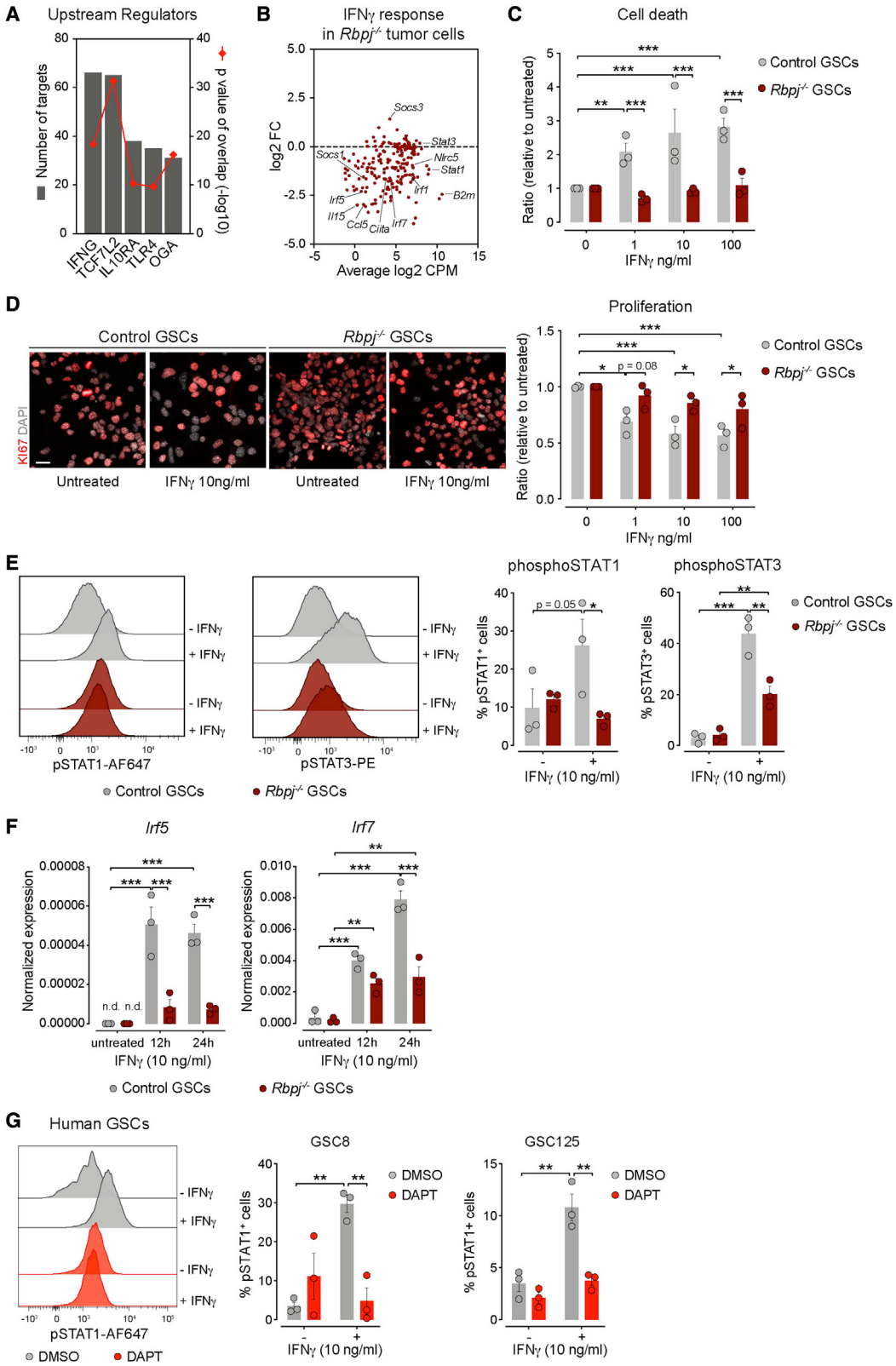

Figure 6. Notch regulates interferon-γ response of human and murine tumor cells

(A) IPA analysis of upstream regulators of the genes that were significantly downregulated in *Rbpj*$^{-/-}$ tumor cells compared with control tumor cells. The number of target genes for each pathway and the p value of overlap are shown.

(legend continued on next page)

communication between tumor and immune cells adapts and contributes to immune niche evolution and tumor aggressiveness.

Gliomas use various strategies to counteract attack by the host immune system. First, TAMs are "educated" by glioma cells to adopt an immunosuppressive phenotype that promotes tumor growth (Pyonteck et al., 2013; Quail et al., 2016). Second, not only in GBMs but also in lower-grade IDH-mutant gliomas, $CD8^+$ T cells are excluded from the TME, and T cell functions are curtailed, suppressing anti-tumor T cell immunity (Bunse et al., 2018; Chongsathidkiet et al., 2018; Cloughesy et al., 2019; Klemm et al., 2020). We show that Notch signaling enhances immune cell infiltration to brain tumors. Conversely, ablating Notch signaling results in an attenuated glioma cell secretome that correlates with reduced homeostatic MG typical of the healthy brain and a reciprocal increase in pro-tumorigenic TAMs. Furthermore, ablating Notch signaling profoundly reduces the T cell content in early-stage gliomas, which is accompanied by increased glioma cell proliferation. Antibody-mediated depletion of T cells before glioma formation mimics the effects of Notch inhibition on tumor cell proliferation, rerouting the importance of T cells to glioma initiation and highlighting the relevance of the pro-tumorigenic niche that Notch inhibition sculpts at early stages of the disease. Therefore, glioma cells can reduce intrinsic Notch activity to exclude subsets of immune cells from the tumor niche, facilitating evasion from immune predation and immune-mediated cytostatic activities. This tumor-suppressive effect of Notch in early tumors is antithetical to the impact that oncogenic Notch can have on the TME in advanced tumors, whereby Notch signaling supports the recruitment of pro-tumorigenic immune infiltrates by amplifying the cancer cell secretome (Jackstadt et al., 2019; Shen et al., 2017).

In GBM, a mesenchymal signature has been linked to a myeloid-rich TME (Gangoso et al., 2021; Hara et al., 2021; Schmitt et al., 2021; Wang et al., 2017). However, the relative absence of immune infiltration in proneural GBM, particularly upon recurrence, remains largely unexplained (Wang et al., 2017). We hypothesize that proneural tumors can undergo mesenchymal switching but can also shape an immunosuppressive niche through an alternative route. This route leads to a moderate myeloid infiltration, a bias in favor of MDMs, and T cell exclusion. We demonstrate that Notch downregulation plays a key role in this phenotypic adaptation. Interestingly, reduced Notch signaling is associated with poor patient outcome in IDH wild-type proneural GBM, even in the absence of mutations in components of the Notch pathway, as well as in IDH-mutant gliomas, which can carry Notch-inactivating mutations and are also classified as proneural (Aoki et al., 2018; Bai et al., 2016; Giachino et al., 2015; Halani et al., 2018; Noushmehr et al., 2010; Verhaak et al., 2010).

Our TAM and T cell depletion experiments indicate that Notch inhibition uncouples the growth of proneural glioma cells from their immune niche. Notably, the Notch1 receptor maintains GSCs in perivascular, hypoxic, and white matter niches, suggesting a universal role of Notch signaling in regulating tumor cell-niche cross-talk in glioma (Jung et al., 2021; Man et al., 2018; Wang et al., 2019). However, GBM cells can compensate for Notch1 downregulation by growing as multicellular networks away from blood vessels, emphasizing that proficient Notch is not an absolute requirement for glioma growth (Jung et al., 2021). We identify a mechanism that underpins immune niche-independent growth of proneural glioma cells upon Notch inhibition. Remarkably, we found that Notch-deficiency in tumor cells counteracts the effects of TAM "re-education" and hinders tumor eradication induced by CSF-1R inhibition. These findings have direct implications for the resistance to TME-targeted therapies, including immunotherapy. Glioma recurrence after the pharmacological "re-education" of TAMs has been observed in long-term preclinical trials (Quail et al., 2016). We speculate that a reduced Notch signal in tumor cells could be one root cause of this phenomenon in some contexts.

Notch signaling can promote stem cell character and drug tolerance, which certainly play roles in its oncogenic function in glioma (Charles et al., 2010; Fan et al., 2010; Funato et al., 2021; Liau et al., 2017; Man et al., 2018; Wang et al., 2019). However, data from human tumors and experimental brain cancer models indicate that reduced Notch signaling is associated with a more aggressive and less quiescent tumor cell phenotype in disease subtypes (Aoki et al., 2018; Bai et al., 2016; Cancer Genome Atlas Research Network et al., 2015; Giachino et al., 2015; Halani et al., 2018; Liau et al., 2017; Nowell and Radtke, 2017; Somasundaram et al., 2005; Suzuki et al., 2015). Although these data imply a tumor-suppressive function of Notch, the underlying molecular mechanisms remained unclear. We demonstrate that by lowering intrinsic Notch activity, proneural glioma cells concurrently boost immune evasion through the attenuation of the IFNγ response and increase their proliferation through the upregulation of oncogenes, thereby reducing growth dependence upon the immune niche (Figure 7F). This immune niche-driven, inverse correlation between proliferation and Notch/IFNγ signaling pathways recalls the neurogenic niche during aging, where infiltrating T cells keep division of Notch-high NSCs in check via IFNγ release (Dulken et al., 2019). We show that particularly Notch1 represses pro-mitotic responses of glioma cells. Notch2, which also acts as a tumor suppressor in the same tumors and is co-expressed with Notch1, does not directly

(B) MA plot of IFNγ response gene signature in *Rbpj*$^{-/-}$ versus control gliomas.
(C) Dose-response analysis of cell death (7-AAD staining) in *Rbpj*$^{-/-}$ and control GSC cultures treated with increasing concentrations of IFNγ (n = 3).
(D) Images of cell proliferation and quantification of KI67 in *Rbpj*$^{-/-}$ and control GSC cultures treated with increasing concentrations of IFNγ (n = 3).
(E) Phospho-flow analysis and quantification of activation (phosphorylation) of IFNγ pathway components STAT1 and STAT3 in *Rbpj*$^{-/-}$ and control GSC lines (n = 3).
(F) qPCR analysis of IFNγ-dependent activation of *Irf5* and *Irf7* expression in *Rbpj*$^{-/-}$ and control GSC cultures over time (n = 3).
(G) Phospho-flow analysis and quantification of activation (phosphorylation) of STAT1 in human GSC8 and GSC125 GBM cells after treatment with IFNγ and the Notch inhibitor DAPT (n = 3).
Data represent mean ± SEM. *p < 0.05, **p < 0.01, ***p < 0.001. Two-way ANOVA with Šídák's (between genotypes) or Tukey's (between concentrations/times) multiple comparisons test (C, D, and F), and two-way ANOVA with Šídák's multiple comparisons test (E and G). Scale bars, 20 μm (D).
See also Figure S6 and Table S5.

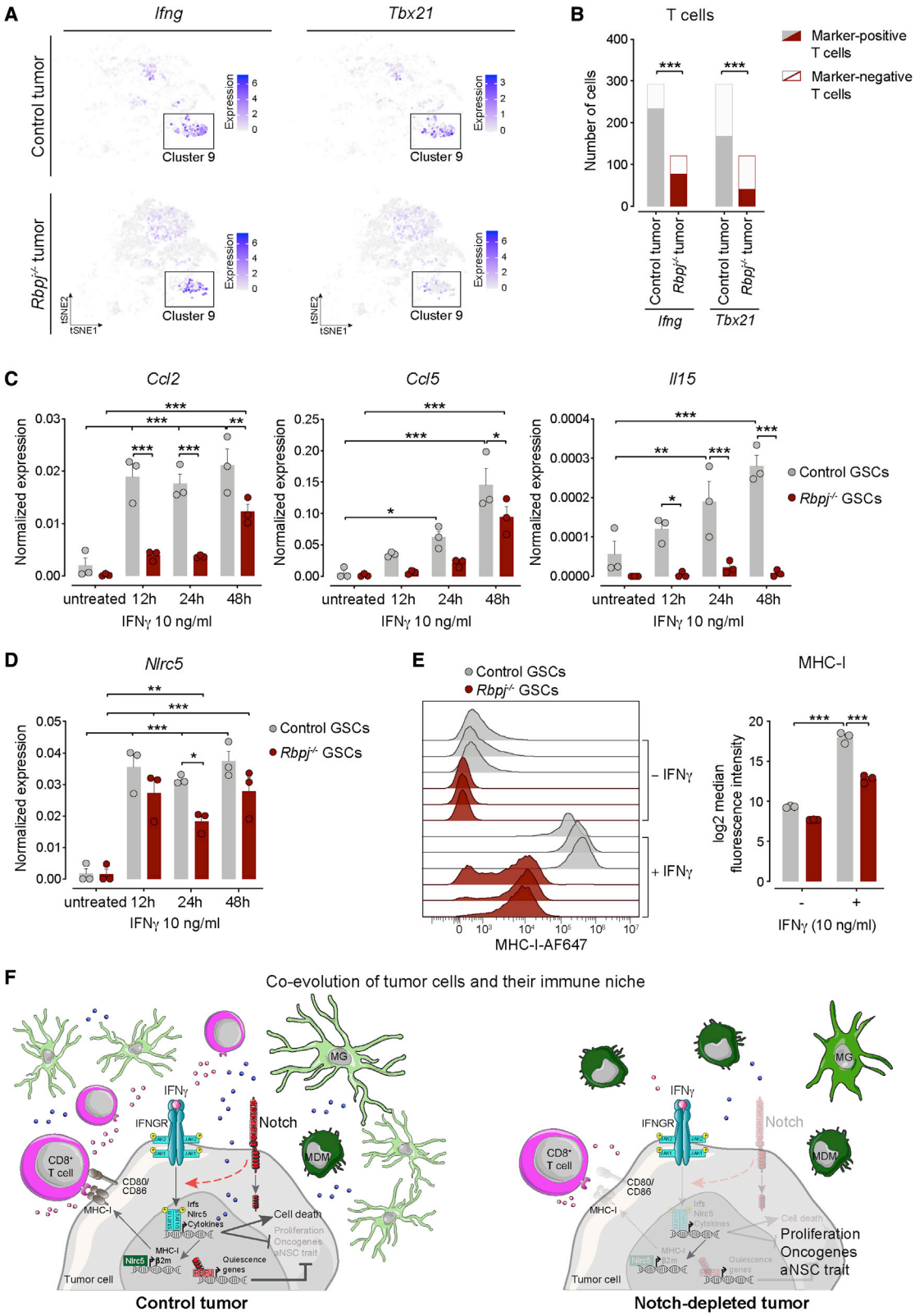

Figure 7. Blunted IFNγ response in tumor cells with reduced Notch activity promotes immune evasion

(A) Visualization of immune cells expressing *Ifng* or *Tbx21* (T-bet) on t-SNE plots of scRNA-sequenced CD45$^+$ cells (see also Figures 2C-2E). T cells are mainly within cluster 9 (highlighted). Normalized $\log_2$ counts were used as a measure for gene expression level.

(legend continued on next page)

impinge on tumor cell proliferation or affect oncogene levels. Both Notch1 and Notch2 induce the expression of immune-regulatory molecules in glioma cells, with Notch2 preferentially affecting components of the antigen processing and presentation machinery. Despite the consistent downregulation of antigen processing and presentation molecules in *Notch2*$^{-/-}$ cells, *Notch1*$^{-/-}$ tumors were more aggressive *in vivo*. We propose this is due to the combination of blunted cytokine production and increased cell proliferation caused by loss of *Notch1*. Although we cannot exclude a contribution of *Notch3* or Notch-independent activities of *Rbpj* to glioma growth, the similarity between *Notch1*$^{-/-}$*Notch2*$^{-/-}$ and *Rbpj*$^{-/-}$ mutant gliomas suggests that *Notch1* and *Notch2* canonical signals play a major role in our tumor model (Kawai et al., 2017; Xie et al., 2016).

Our analyses of human glioma datasets and GBM stem cell lines show that Notch-inactivating mutations and Notch signaling levels affect IFNγ signaling and inflammatory responses in patients and immunocompetent preclinical models of glioma. We found that Notch strengthens IFNγ response by tumor cells at multiple levels, modulating STAT phosphorylation and the expression of IFNγ targets including IRFs, cytokines, and MHC-I components. Glioma cells where Notch signaling is abrogated are refractory to the cytostatic and cytotoxic effects of IFNγ. Notably, IFNγ-dependent MHC-I expression is prevented after Notch ablation from glioma cells, eventually impairing antigen presentation and promoting escape from immune attack. In direct support for this, a recent CRISPR screen identified Notch1 receptor and B2M, an essential component of the MHC-I complex, as frequently co-mutated functional tumor suppressors driving gliomagenesis *in vivo* (Chow et al., 2017). Notch-depleted glioma cells also feature blunted cytokine production downstream of IFNγ stimulation. As T cells are a major source of IFNγ, a reduced cytokine production by glioma cells after Notch inhibition directly diminishes attraction and infiltration of lymphocytes to the tumor, thereby reducing the source of IFNγ *in vivo*. The reduced IFNγ levels in the TME further decrease IFNγ response of Notch-depleted tumor cells, unveiling a Notch-regulated non-cell-autonomous inhibitory feedback loop that promotes immune evasion and immune niche coercion (Figure 7F). Although the molecular details of the Notch/IFN interaction in glioma deserve further scrutiny, previous reports suggest that Notch can boost STAT activation and IRF expression in NSCs and macrophages, respectively (Kamakura et al., 2004; Xu et al., 2012). It would be important to determine whether a similar cross-talk between Notch and IFN occurs in other tumor types, such as small cell lung cancer, where elevated Notch signaling positively correlates with the response to immunotherapy (Roper et al., 2021).

Loss of Notch signaling induces transcriptional programs typical of aNSCs and the expression of oncogenes by glioma cells, which we propose could further enhance immune niche-independent growth. Particularly, we observed augmented MYC-driven proliferation in Notch-depleted gliomas, reminiscent of loss of quiescence after Notch inhibition in NSCs, an important cell type of origin of glioma (Alcantara Llaguno et al., 2009; Engler et al., 2018; Imayoshi et al., 2010; Zhang et al., 2019). Enhanced MYC has also been linked to an immunosuppressive TME and reduced antigen presentation in lung cancer, suggesting that MYC could antagonize some effects of IFN signaling and determine the local immunophenotype in glioma as well (Kortlever et al., 2017; Topper et al., 2017). Although MYC is a well-known transcriptional target of oncogenic Notch in some forms of leukemia, Notch inhibition can induce MYC-dependent mitogenic and metabolic activities in endothelial cells, and HES5 can suppress MYC-dependent hepatocarcinogenesis (Fabbri et al., 2011; Herranz et al., 2014; Luiken et al., 2020; Luo et al., 2021; Nowell and Radtke, 2017). Thus, paradoxically, context-dependent regulation of MYC could play a role in both oncogenic and tumor-suppressive effects of Notch signaling in different cancers.

Cell-to-cell variation in Notch signaling intensity can contribute to intra-tumor heterogeneity (Charles et al., 2010; Liau et al., 2017). In support of this, the Notch pathway can act both as an oncogene and a tumor suppressor in glioma (Jung et al., 2021; Parmigiani et al., 2020). Therefore, Notch could exert dual roles even within the same tumor, for instance, by promoting stem cell character but simultaneously repressing proliferation and immune evasion. Although Notch activation delays initial glioma progression, it could provide a survival advantage to some cell populations after chemotherapy and fuel tumor relapse. A similar intratumoral heterogeneity with divergent functions of Notch in distinct cell subpopulations and at different stages of tumor development has been shown in small cell lung cancer (Lim et al., 2017).

Altogether, our findings indicate that changes in Notch activity in proneural glioma cells regulate activated stem cell trait, tumor niche strength, and acquired immune evasion by coordinating local feedback between glioma and immune cells.

Limitations of the study

Analysis of more human cell lines and mouse models will allow to determine whether the mechanisms that we have identified in proneural tumors play a role in the development of other glioma

(B) Quantification of T cells expressing *Ifng* or *Tbx21* in *Rbpj*$^{-/-}$ and control gliomas. Data are extracted from scRNA-seq analysis of CD45^{+} cells.
(C) qPCR analysis of IFNγ-dependent activation of cytokine expression by *Rbpj*$^{-/-}$ and control GSC cultures over time (n = 3).
(D) qPCR analysis of IFNγ-dependent activation of *Nlrc5* expression by *Rbpj*$^{-/-}$ and control GSC cultures over time (n = 3).
(E) Flow cytometry analysis and quantification of IFNγ-dependent cell surface expression levels of MHC-I molecules in *Rbpj*$^{-/-}$ and control GSC cultures. 3 independent GSC lines for each genotype are shown in the flow cytometry histogram.
(F) Blunted IFNγ-response in tumor cells and reduced recruitment of IFNγ-producing immune cell populations establish an inhibitory feedback loop that promotes immune evasion and aggressiveness of proneural gliomas with low Notch activity. The TME of Notch-inhibited tumors is depleted of T lymphocytes and homeostatic MG-like TAMs and enriched in immunosuppressive TAM populations. This coincides with downregulation of genes that promote proliferative quiescence, upregulation of oncogenes and transcriptional programs typical of aNSCs, and ultimately uncoupling of tumor growth from the immune niche.
Data represent mean ± SEM. *p < 0.05, **p < 0.01, ***p < 0.001. Fisher's exact test (B), two-way ANOVA with Šídák's (between genotypes/treatments) or Tukey's (between times) multiple comparisons test (C–E).
See also Figure S7.

subtypes. Further work is also needed to explore the extent to which Notch inhibition represents an immune escape mechanism in other cancers and whether modulating Notch could be an attractive therapeutic strategy to release anti-tumor immunity in some cancer types.

STAR★METHODS

Detailed methods are provided in the online version of this paper and include the following:

- KEY RESOURCES TABLE
- RESOURCE AVAILABILITY
  - Lead contact
  - Materials availability
  - Data and code availability
- EXPERIMENTAL MODEL AND SUBJECT DETAILS
  - Animal models
  - Cell Lines
- METHOD DETAILS
  - Retroviral constructs, retroviral transduction and generation of murine gliomas
  - CSF-1R inhibitor administration
  - *In vivo* depletion of T lymphocytes
  - Immunostaining of brain tissue and cell cultures
  - Tumor isolation, fluorescence activated cell sorting (FACS) and flow cytometry
  - GSCs and microglia cell cultures
  - Total cell protein extraction and western blotting
  - Phosphoflow cytometry
  - RNA isolation and quantitative reverse-transcriptase PCR
  - RNA-seq
  - Switch analysis
  - Gene pathways enrichment analyses
  - Analysis of human glioma datasets
- QUANTIFICATION AND STATISTICAL ANALYSIS

SUPPLEMENTAL INFORMATION

Supplemental information can be found online at https://doi.org/10.1016/j.devcel.2022.06.006.

ACKNOWLEDGMENTS

We thank the members of the Taylor lab for critical reading of the manuscript and Karin Burger and Frank Sager for excellent technical assistance. We thank Christian Beisel, Katja Eschbach, Tobias Schär, and the Quantitative Genomics Facility of the Department of Biosystems Science and Engineering of ETH Zürich in Basel for performing the sequencing experiments. We are grateful to Pascal Lorentz and the DBM Microscopy Core Facility for support with microscopy. Calculations were performed at sciCORE (http://scicore.unibas.ch/) scientific computing core facility at University of Basel. This work was supported by the Swiss Cancer League (KFS-3600-02-2015 and KLS-4518-08-2018), the Stiftung zur Krebsbekämpfung, the Huggenberger-Bischoff Stiftung zur Krebsforschung, the Novartis foundation for medical-biological research, the Stiftung für krebskranke Kinder Regio Basiliensis, the Stiftung Tumorforschung Kopf-Hals, the Forschungsfonds Nachwuchsforschende of the University of Basel, and the Swiss National Science Foundation (31003A_162609 and 31003A_182388).

AUTHOR CONTRIBUTIONS

E.P. and C.G. performed experiments. C.R., R.T., G.T., and F.M.L. helped with the design of flow cytometry and FACS experiments. K.H. provided antibodies and helped with the design of T cell depletion experiments. E.P., C.G., V.T., R.T., G.T., F.M.L., S.F., L.M., and G.H. interpreted the data. R.I. and E.P. performed bioinformatics analyses. S.B., S.C.M., A.L., M.G., R.T., D.F., A.G., G.H., and H.W. provided material and evaluated the data. S.F. evaluated histopathological analyses. C.G., V.T., and E.P. acquired funding. C.G. and V.T. supervised the project. C.G. and E.P. conceived and designed the project, prepared the figures, and wrote the paper. All authors edited or commented on the manuscript.

DECLARATION OF INTERESTS

S.C.M. has consulted for and received honoraria from Celgene/BMS and Novartis.

Received: November 16, 2021
Revised: May 4, 2022
Accepted: June 10, 2022
Published: July 7, 2022

REFERENCES

Alcantara Llaguno, S., Chen, J., Kwon, C.H., Jackson, E.L., Li, Y., Burns, D.K., Alvarez-Buylla, A., and Parada, L.F. (2009). Malignant astrocytomas originate from neural stem/progenitor cells in a somatic tumor suppressor mouse model. Cancer Cell *15*, 45–56.

Aoki, K., Nakamura, H., Suzuki, H., Matsuo, K., Kataoka, K., Shimamura, T., Motomura, K., Ohka, F., Shiina, S., Yamamoto, T., et al. (2018). Prognostic relevance of genetic alterations in diffuse lower-grade gliomas. Neuro. Oncol. *20*, 66–77.

Ashburner, M., Ball, C.A., Blake, J.A., Botstein, D., Butler, H., Cherry, J.M., Davis, A.P., Dolinski, K., Dwight, S.S., Eppig, J.T., et al. (2000). Gene ontology: tool for the unification of biology. The Gene Ontology Consortium. Nat. Genet. *25*, 25–29.

Azizi, E., Carr, A.J., Plitas, G., Cornish, A.E., Konopacki, C., Prabhakaran, S., Nainys, J., Wu, K., Kiseliovas, V., Setty, M., et al. (2018). Single-cell map of diverse immune phenotypes in the breast tumor microenvironment. Cell *174*, 1293–1308.e36.

Bai, H., Harmancı, A.S., Erson-Omay, E.Z., Li, J., Coşkun, S., Simon, M., Krischek, B., Özduman, K., Omay, S.B., Sorensen, E.A., et al. (2016). Integrated genomic characterization of IDH1-mutant glioma malignant progression. Nat. Genet. *48*, 59–66.

Barrow, A.D., Edeling, M.A., Trifonov, V., Luo, J., Goyal, P., Bohl, B., Bando, J.K., Kim, A.H., Walker, J., Andahazy, M., et al. (2018). Natural killer cells control tumor growth by sensing a growth factor. Cell *172*, 534–548.e19.

Bernstein, I.D., Tam, M.R., and Nowinski, R.C. (1980). Mouse leukemia: therapy with monoclonal antibodies against a thymus differentiation antigen. Science *207*, 68–71.

Besseyrias, V., Fiorini, E., Strobl, L.J., Zimber-Strobl, U., Dumortier, A., Koch, U., Arcangeli, M.L., Ezine, S., Macdonald, H.R., and Radtke, F. (2007). Hierarchy of Notch-Delta interactions promoting T cell lineage commitment and maturation. J. Exp. Med. *204*, 331–343.

Binnewies, M., Roberts, E.W., Kersten, K., Chan, V., Fearon, D.F., Merad, M., Coussens, L.M., Gabrilovich, D.I., Ostrand-Rosenberg, S., Hedrick, C.C., et al. (2018). Understanding the tumor immune microenvironment (TIME) for effective therapy. Nat. Med. *24*, 541–550.

Bowman, R.L., Klemm, F., Akkari, L., Pyonteck, S.M., Sevenich, L., Quail, D.F., Dhara, S., Simpson, K., Gardner, E.E., Iacobuzio-Donahue, C.A., et al. (2016). Macrophage ontogeny underlies differences in tumor-specific education in brain malignancies. Cell Rep. *17*, 2445–2459.

Bunse, L., Pusch, S., Bunse, T., Sahm, F., Sanghvi, K., Friedrich, M., Alansary, D., Sonner, J.K., Green, E., Deumelandt, K., et al. (2018). Suppression of

antitumor T cell immunity by the oncometabolite (R)-2-hydroxyglutarate. Nat. Med. *24*, 1192–1203.

Butovsky, O., Jedrychowski, M.P., Moore, C.S., Cialic, R., Lanser, A.J., Gabriely, G., Koeglsperger, T., Dake, B., Wu, P.M., Doykan, C.E., et al. (2014). Identification of a unique TGF-beta-dependent molecular and functional signature in microglia. Nat. Neurosci. *17*, 131–143.

Cancer Genome Atlas Research Network, Brat, D.J., Verhaak, R.G., Aldape, K.D., Yung, W.K., Salama, S.R., Cooper, L.A., Rheinbay, E., Miller, C.R., Vitucci, M., et al. (2015). Comprehensive, integrative genomic analysis of diffuse lower-grade gliomas. N. Engl. J. Med. *372*, 2481–2498.

Capper, D., Jones, D.T.W., Sill, M., Hovestadt, V., Schrimpf, D., Sturm, D., Koelsche, C., Sahm, F., Chavez, L., Reuss, D.E., et al. (2018). DNA methylation-based classification of central nervous system tumours. Nature *555*, 469–474.

Charles, N., Ozawa, T., Squatrito, M., Bleau, A.M., Brennan, C.W., Hambardzumyan, D., and Holland, E.C. (2010). Perivascular nitric oxide activates notch signaling and promotes stem-like character in PDGF-induced glioma cells. Cell Stem Cell *6*, 141–152.

Chongsathidkiet, P., Jackson, C., Koyama, S., Loebel, F., Cui, X., Farber, S.H., Woroniecka, K., Elsamadicy, A.A., Dechant, C.A., Kemeny, H.R., et al. (2018). Sequestration of T cells in bone marrow in the setting of glioblastoma and other intracranial tumors. Nat. Med. *24*, 1459–1468.

Chow, R.D., Guzman, C.D., Wang, G., Schmidt, F., Youngblood, M.W., Ye, L., Errami, Y., Dong, M.B., Martinez, M.A., Zhang, S., et al. (2017). AAV-mediated direct in vivo CRISPR screen identifies functional suppressors in glioblastoma. Nat. Neurosci. *20*, 1329–1341.

Cloughesy, T.F., Mochizuki, A.Y., Orpilla, J.R., Hugo, W., Lee, A.H., Davidson, T.B., Wang, A.C., Ellingson, B.M., Rytlewski, J.A., Sanders, C.M., et al. (2019). Neoadjuvant anti-PD-1 immunotherapy promotes a survival benefit with intratumoral and systemic immune responses in recurrent glioblastoma. Nat. Med. *25*, 477–486.

Codega, P., Silva-Vargas, V., Paul, A., Maldonado-Soto, A.R., Deleo, A.M., Pastrana, E., and Doetsch, F. (2014). Prospective identification and purification of quiescent adult neural stem cells from their *in vivo* niche. Neuron *82*, 545–559.

Dialynas, D.P., Quan, Z.S., Wall, K.A., Pierres, A., Quintáns, J., Loken, M.R., Pierres, M., and Fitch, F.W. (1983). Characterization of the murine T cell surface molecule, designated L3T4, identified by monoclonal antibody GK1.5: similarity of L3T4 to the human Leu-3/T4 molecule. J. Immunol. *131*, 2445–2451.

Dulken, B.W., Buckley, M.T., Navarro Negredo, P., Saligrama, N., Cayrol, R., Leeman, D.S., George, B.M., Boutet, S.C., Hebestreit, K., Pluvinage, J.V., et al. (2019). Single-cell analysis reveals T cell infiltration in old neurogenic niches. Nature *571*, 205–210.

Engler, A., Rolando, C., Giachino, C., Saotome, I., Erni, A., Brien, C., Zhang, R., Zimber-Strobl, U., Radtke, F., Artavanis-Tsakonas, S., et al. (2018). Notch2 signaling maintains NSC quiescence in the murine ventricular-subventricular zone. Cell Rep. *22*, 992–1002.

Fabbri, G., Rasi, S., Rossi, D., Trifonov, V., Khiabanian, H., Ma, J., Grunn, A., Fangazio, M., Capello, D., Monti, S., et al. (2011). Analysis of the chronic lymphocytic leukemia coding genome: role of NOTCH1 mutational activation. J. Exp. Med. *208*, 1389–1401.

Fan, X., Khaki, L., Zhu, T.S., Soules, M.E., Talsma, C.E., Gul, N., Koh, C., Zhang, J., Li, Y.M., Maciaczyk, J., et al. (2010). NOTCH pathway blockade depletes CD133-positive glioblastoma cells and inhibits growth of tumor neurospheres and xenografts. Stem Cells *28*, 5–16.

Friebel, E., Kapolou, K., Unger, S., Núñez, N.G., Utz, S., Rushing, E.J., Regli, L., Weller, M., Greter, M., Tugues, S., et al. (2020). Single-cell mapping of human brain cancer reveals tumor-specific instruction of tissue-invading leukocytes. Cell *181*, 1626–1642.e20.

Funato, K., Smith, R.C., Saito, Y., and Tabar, V. (2021). Dissecting the impact of regional identity and the oncogenic role of human-specific NOTCH2NL in an hESC model of H3.3G34R-mutant glioma. Cell Stem Cell *28*, 894–905.e7.

Gangoso, E., Southgate, B., Bradley, L., Rus, S., Galvez-Cancino, F., McGivern, N., Güç, E., Kapourani, C.A., Byron, A., Ferguson, K.M., et al. (2021). Glioblastomas acquire myeloid-affiliated transcriptional programs via epigenetic immunoediting to elicit immune evasion. Cell *184*, 2454–2470.e26.

Giachino, C., Boulay, J.L., Ivanek, R., Alvarado, A., Tostado, C., Lugert, S., Tchorz, J., Coban, M., Mariani, L., Bettler, B., et al. (2015). A tumor suppressor function for notch signaling in forebrain tumor subtypes. Cancer Cell *28*, 730–742.

Halani, S.H., Yousefi, S., Velazquez Vega, J., Rossi, M.R., Zhao, Z., Amrollahi, F., Holder, C.A., Baxter-Stoltzfus, A., Eschbacher, J., Griffith, B., et al. (2018). Multi-faceted computational assessment of risk and progression in oligodendroglioma implicates NOTCH and PI3K pathways. NPJ Precis. Oncol. *2*, 24.

Han, H., Tanigaki, K., Yamamoto, N., Kuroda, K., Yoshimoto, M., Nakahata, T., Ikuta, K., and Honjo, T. (2002). Inducible gene knockout of transcription factor recombination signal binding protein-J reveals its essential role in T versus B lineage decision. Int. Immunol. *14*, 637–645.

Hara, T., Chanoch-Myers, R., Mathewson, N.D., Myskiw, C., Atta, L., Bussema, L., Eichhorn, S.W., Greenwald, A.C., Kinker, G.S., Rodman, C., et al. (2021). Interactions between cancer cells and immune cells drive transitions to mesenchymal-like states in glioblastoma. Cancer Cell *39*, 779–792.e11.

Herranz, D., Ambesi-Impiombato, A., Palomero, T., Schnell, S.A., Belver, L., Wendorff, A.A., Xu, L., Castillo-Martin, M., Llobet-Navás, D., Cordon-Cardo, C., et al. (2014). A NOTCH1-driven MYC enhancer promotes T cell development, transformation and acute lymphoblastic leukemia. Nat. Med. *20*, 1130–1137.

Hildner, K., Edelson, B.T., Purtha, W.E., Diamond, M., Matsushita, H., Kohyama, M., Calderon, B., Schraml, B.U., Unanue, E.R., Diamond, M.S., et al. (2008). Batf3 deficiency reveals a critical role for CD8alpha+ dendritic cells in cytotoxic T cell immunity. Science *322*, 1097–1100.

Imayoshi, I., Sakamoto, M., Yamaguchi, M., Mori, K., and Kageyama, R. (2010). Essential roles of Notch signaling in maintenance of neural stem cells in developing and adult brains. J. Neurosci. *30*, 3489–3498.

Jackson, C.M., Choi, J., and Lim, M. (2019). Mechanisms of immunotherapy resistance: lessons from glioblastoma. Nat. Immunol. *20*, 1100–1109.

Jackstadt, R., van Hooff, S.R., Leach, J.D., Cortes-Lavaud, X., Lohuis, J.O., Ridgway, R.A., Wouters, V.M., Roper, J., Kendall, T.J., Roxburgh, C.S., et al. (2019). Epithelial NOTCH signaling rewires the tumor microenvironment of colorectal cancer to drive poor-prognosis subtypes and metastasis. Cancer Cell *36*, 319–336.e7.

Jonkers, J., Meuwissen, R., van der Gulden, H., Peterse, H., van der Valk, M., and Berns, A. (2001). Synergistic tumor suppressor activity of BRCA2 and p53 in a conditional mouse model for breast cancer. Nat. Genet. *29*, 418–425.

Jung, E., Osswald, M., Ratliff, M., Dogan, H., Xie, R., Weil, S., Hoffmann, D.C., Kurz, F.T., Kessler, T., Heiland, S., et al. (2021). Tumor cell plasticity, heterogeneity, and resistance in crucial microenvironmental niches in glioma. Nat. Commun. *12*, 1014.

Kamakura, S., Oishi, K., Yoshimatsu, T., Nakafuku, M., Masuyama, N., and Gotoh, Y. (2004). Hes binding to STAT3 mediates crosstalk between Notch and JAK-STAT signalling. Nat. Cell Biol. *6*, 547–554.

Kawai, H., Kawaguchi, D., Kuebrich, B.D., Kitamoto, T., Yamaguchi, M., Gotoh, Y., and Furutachi, S. (2017). Area-specific regulation of quiescent neural stem cells by notch3 in the adult mouse subependymal zone. J. Neurosci. *37*, 11867–11880.

Klemm, F., Maas, R.R., Bowman, R.L., Kornete, M., Soukup, K., Nassiri, S., Brouland, J.P., Iacobuzio-Donahue, C.A., Brennan, C., Tabar, V., et al. (2020). Interrogation of the microenvironmental landscape in brain tumors reveals disease-specific alterations of immune cells. Cell *181*, 1643–1660.e17.

Kobayashi, K.S., and van den Elsen, P.J. (2012). NLRC5: a key regulator of MHC class I-dependent immune responses. Nat. Rev. Immunol. *12*, 813–820.

Kortlever, R.M., Sodir, N.M., Wilson, C.H., Burkhart, D.L., Pellegrinet, L., Brown Swigart, L., Littlewood, T.D., and Evan, G.I. (2017). Myc cooperates with Ras by programming inflammation and immune suppression. Cell *171*, 1301–1315.e14.

Ledbetter, J.A., and Herzenberg, L.A. (1979). Xenogeneic monoclonal antibodies to mouse lymphoid differentiation antigens. Immunol. Rev. *47*, 63–90.

Liau, B.B., Sievers, C., Donohue, L.K., Gillespie, S.M., Flavahan, W.A., Miller, T.E., Venteicher, A.S., Hebert, C.H., Carey, C.D., Rodig, S.J., et al. (2017). Adaptive chromatin remodeling drives glioblastoma stem cell plasticity and drug tolerance. Cell Stem Cell *20*, 233–246.e7.

Lim, J.S., Ibaseta, A., Fischer, M.M., Cancilla, B., O'Young, G., Cristea, S., Luca, V.C., Yang, D., Jahchan, N.S., Hamard, C., et al. (2017). Intratumoural heterogeneity generated by Notch signalling promotes small-cell lung cancer. Nature *545*, 360–364.

Lim, M., Xia, Y., Bettegowda, C., and Weller, M. (2018). Current state of immunotherapy for glioblastoma. Nat. Rev. Clin. Oncol. *15*, 422–442.

Lugert, S., Basak, O., Knuckles, P., Haussler, U., Fabel, K., Götz, M., Haas, C.A., Kempermann, G., Taylor, V., and Giachino, C. (2010). Quiescent and active hippocampal neural stem cells with distinct morphologies respond selectively to physiological and pathological stimuli and aging. Cell Stem Cell *6*, 445–456.

Luiken, S., Fraas, A., Bieg, M., Sugiyanto, R., Goeppert, B., Singer, S., Ploeger, C., Warsow, G., Marquardt, J.U., Sticht, C., et al. (2020). NOTCH target gene HES5 mediates oncogenic and tumor suppressive functions in hepatocarcinogenesis. Oncogene *39*, 3128–3144.

Lun, A.T.L., and Marioni, J.C. (2017). Overcoming confounding plate effects in differential expression analyses of single-cell RNA-seq data. Biostatistics *18*, 451–464.

Luo, W., Garcia-Gonzalez, I., Fernández-Chacón, M., Casquero-Garcia, V., Sanchez-Muñoz, M.S., Mühleder, S., Garcia-Ortega, L., Andrade, J., Potente, M., and Benedito, R. (2021). Arterialization requires the timely suppression of cell growth. Nature *589*, 437–441.

Man, J., Yu, X., Huang, H., Zhou, W., Xiang, C., Miele, L., Liu, Z., Bebek, G., Bao, S., and Yu, J.S. (2018). Hypoxic induction of vasorin regulates Notch1 turnover to maintain glioma stem-like cells. Cell Stem Cell *22*, 104–118.e6.

Mehta, S., Huillard, E., Kesari, S., Maire, C.L., Golebiowski, D., Harrington, E.P., Alberta, J.A., Kane, M.F., Theisen, M., Ligon, K.L., et al. (2011). The central nervous system-restricted transcription factor Olig2 opposes p53 responses to genotoxic damage in neural progenitors and malignant glioma. Cancer Cell *19*, 359–371.

Monaco, G., Lee, B., Xu, W., Mustafah, S., Hwang, Y.Y., Carré, C., Burdin, N., Visan, L., Ceccarelli, M., Poidinger, M., et al. (2019). RNA-seq signatures normalized by mRNA abundance allow absolute deconvolution of human immune cell types. Cell Rep. *26*, 1627–1640.e7.

Naik, S., Larsen, S.B., Cowley, C.J., and Fuchs, E. (2018). Two to tango: dialog between immunity and stem cells in health and disease. Cell *175*, 908–920.

Neftel, C., Laffy, J., Filbin, M.G., Hara, T., Shore, M.E., Rahme, G.J., Richman, A.R., Silverbush, D., Shaw, M.L., Hebert, C.M., et al. (2019). An integrative model of cellular states, plasticity, and genetics for glioblastoma. Cell *178*, 835–849.e21.

Noushmehr, H., Weisenberger, D.J., Diefes, K., Phillips, H.S., Pujara, K., Berman, B.P., Pan, F., Pelloski, C.E., Sulman, E.P., Bhat, K.P., et al. (2010). Identification of a CpG island methylator phenotype that defines a distinct subgroup of glioma. Cancer Cell *17*, 510–522.

Nowell, C.S., and Radtke, F. (2017). Notch as a tumour suppressor. Nat. Rev. Cancer *17*, 145–159.

Ozawa, T., Riester, M., Cheng, Y.K., Huse, J.T., Squatrito, M., Helmy, K., Charles, N., Michor, F., and Holland, E.C. (2014). Most human non-GCIMP glioblastoma subtypes evolve from a common proneural-like precursor glioma. Cancer Cell *26*, 288–300.

Parmigiani, E., Taylor, V., and Giachino, C. (2020). Oncogenic and tumor-suppressive functions of NOTCH signaling in glioma. Cells *9*, e2304.

Phillips, H.S., Kharbanda, S., Chen, R., Forrest, W.F., Soriano, R.H., Wu, T.D., Misra, A., Nigro, J.M., Colman, H., Soroceanu, L., et al. (2006). Molecular subclasses of high-grade glioma predict prognosis, delineate a pattern of disease progression, and resemble stages in neurogenesis. Cancer Cell *9*, 157–173.

Prager, B.C., Xie, Q., Bao, S., and Rich, J.N. (2019). Cancer stem cells: the architects of the tumor ecosystem. Cell Stem Cell *24*, 41–53.

Pyonteck, S.M., Akkari, L., Schuhmacher, A.J., Bowman, R.L., Sevenich, L., Quail, D.F., Olson, O.C., Quick, M.L., Huse, J.T., Teijeiro, V., et al. (2013). CSF-1R inhibition alters macrophage polarization and blocks glioma progression. Nat. Med. *19*, 1264–1272.

Quail, D.F., Bowman, R.L., Akkari, L., Quick, M.L., Schuhmacher, A.J., Huse, J.T., Holland, E.C., Sutton, J.C., and Joyce, J.A. (2016). The tumor microenvironment underlies acquired resistance to CSF-1R inhibition in gliomas. Science *352*, aad3018.

Radtke, F., Wilson, A., Stark, G., Bauer, M., van Meerwijk, J., MacDonald, H.R., and Aguet, M. (1999). Deficient T cell fate specification in mice with an induced inactivation of Notch1. Immunity *10*, 547–558.

Roper, N., Velez, M.J., Chiappori, A., Kim, Y.S., Wei, J.S., Sindiri, S., Takahashi, N., Mulford, D., Kumar, S., Ylaya, K., et al. (2021). Notch signaling and efficacy of PD-1/PD-L1 blockade in relapsed small cell lung cancer. Nat. Commun. *12*, 3880.

Schalper, K.A., Rodriguez-Ruiz, M.E., Diez-Valle, R., López-Janeiro, A., Porciuncula, A., Idoate, M.A., Inogés, S., de Andrea, C., López-Diaz de Cerio, A., Tejada, S., et al. (2019). Neoadjuvant nivolumab modifies the tumor immune microenvironment in resectable glioblastoma. Nat. Med. *25*, 470–476.

Schindelin, J., Arganda-Carreras, I., Frise, E., Kaynig, V., Longair, M., Pietzsch, T., Preibisch, S., Rueden, C., Saalfeld, S., Schmid, B., et al. (2012). Fiji: an open-source platform for biological-image analysis. Nat. Methods *9*, 676–682.

Schmitt, M.J., Company, C., Dramaretska, Y., Barozzi, I., Göhrig, A., Kertalli, S., Großmann, M., Naumann, H., Sanchez-Bailon, M.P., Hulsman, D., et al. (2021). Phenotypic mapping of pathologic cross-talk between glioblastoma and innate immune cells by synthetic genetic tracing. Cancer Discov. *11*, 754–777.

Shen, Q., Cohen, B., Zheng, W., Rahbar, R., Martin, B., Murakami, K., Lamorte, S., Thompson, P., Berman, H., Zúñiga-Pflücker, J.C., et al. (2017). Notch shapes the innate immunophenotype in breast cancer. Cancer Discov. *7*, 1320–1335.

Somasundaram, K., Reddy, S.P., Vinnakota, K., Britto, R., Subbarayan, M., Nambiar, S., Hebbar, A., Samuel, C., Shetty, M., Sreepathi, H.K., et al. (2005). Upregulation of ASCL1 and inhibition of Notch signaling pathway characterize progressive astrocytoma. Oncogene *24*, 7073–7083.

Suzuki, H., Aoki, K., Chiba, K., Sato, Y., Shiozawa, Y., Shiraishi, Y., Shimamura, T., Niida, A., Motomura, K., Ohka, F., et al. (2015). Mutational landscape and clonal architecture in grade II and III gliomas. Nat. Genet. *47*, 458–468.

Tchorz, J.S., Suply, T., Ksiazek, I., Giachino, C., Cloëtta, D., Danzer, C.P., Doll, T., Isken, A., Lemaistre, M., Taylor, V., et al. (2012). A modified RMCE-compatible Rosa26 locus for the expression of transgenes from exogenous promoters. PLoS One *7*, e30011.

Tirosh, I., Venteicher, A.S., Hebert, C., Escalante, L.E., Patel, A.P., Yizhak, K., Fisher, J.M., Rodman, C., Mount, C., Filbin, M.G., et al. (2016). Single-cell RNA-seq supports a developmental hierarchy in human oligodendroglioma. Nature *539*, 309–313.

Topper, M.J., Vaz, M., Chiappinelli, K.B., DeStefano Shields, C.E., Niknafs, N., Yen, R.C., Wenzel, A., Hicks, J., Ballew, M., Stone, M., et al. (2017). Epigenetic therapy ties MYC depletion to reversing immune evasion and treating lung Cancer. Cell *171*, 1284–1300.e21.

Tussiwand, R., Lee, W.L., Murphy, T.L., Mashayekhi, M., Kc, W., Albring, J.C., Satpathy, A.T., Rotondo, J.A., Edelson, B.T., Kretzer, N.M., et al. (2012). Compensatory dendritic cell development mediated by BATF-IRF interactions. Nature *490*, 502–507.

Venteicher, A.S., Tirosh, I., Hebert, C., Yizhak, K., Neftel, C., Filbin, M.G., Hovestadt, V., Escalante, L.E., Shaw, M.L., Rodman, C., et al. (2017). Decoupling genetics, lineages, and microenvironment in IDH-mutant gliomas by single-cell RNA-seq. Science *355*, eaai8478.

Verhaak, R.G., Hoadley, K.A., Purdom, E., Wang, V., Qi, Y., Wilkerson, M.D., Miller, C.R., Ding, L., Golub, T., Mesirov, J.P., et al. (2010). Integrated genomic analysis identifies clinically relevant subtypes of glioblastoma characterized by abnormalities in PDGFRA, IDH1, EGFR, and NF1. Cancer Cell *17*, 98–110.

Wakimoto, H., Kesari, S., Farrell, C.J., Curry, W.T., Jr., Zaupa, C., Aghi, M., Kuroda, T., Stemmer-Rachamimov, A., Shah, K., Liu, T.C., et al. (2009). Human glioblastoma-derived cancer stem cells: establishment of invasive glioma models and treatment with oncolytic herpes simplex virus vectors. Cancer Res. *69*, 3472–3481.

Wang, J., Xu, S.L., Duan, J.J., Yi, L., Guo, Y.F., Shi, Y., Li, L., Yang, Z.Y., Liao, X.M., Cai, J., et al. (2019). Invasion of white matter tracts by glioma stem cells is regulated by a NOTCH1-SOX2 positive-feedback loop. Nat. Neurosci. *22*, 91–105.

Wang, Q., Hu, B., Hu, X., Kim, H., Squatrito, M., Scarpace, L., deCarvalho, A.C., Lyu, S., Li, P., Li, Y., et al. (2017). Tumor evolution of glioma-intrinsic gene expression subtypes associates with immunological changes in the microenvironment. Cancer Cell *32*, 42–56.e6.

Xie, Q., Wu, Q., Kim, L., Miller, T.E., Liau, B.B., Mack, S.C., Yang, K., Factor, D.C., Fang, X., Huang, Z., et al. (2016). RBPJ maintains brain tumor-initiating cells through CDK9-mediated transcriptional elongation. J. Clin. Invest. *126*, 2757–2772.

Xu, H., Zhu, J., Smith, S., Foldi, J., Zhao, B., Chung, A.Y., Outtz, H., Kitajewski, J., Shi, C., Weber, S., et al. (2012). Notch-RBP-J signaling regulates the transcription factor IRF8 to promote inflammatory macrophage polarization. Nat. Immunol. *13*, 642–650.

Yoshihara, K., Shahmoradgoli, M., Martínez, E., Vegesna, R., Kim, H., Torres-Garcia, W., Treviño, V., Shen, H., Laird, P.W., Levine, D.A., et al. (2013). Inferring tumour purity and stromal and immune cell admixture from expression data. Nat. Commun. *4*, 2612.

Zhang, R., Boareto, M., Engler, A., Louvi, A., Giachino, C., Iber, D., and Taylor, V. (2019). Id4 downstream of Notch2 maintains neural stem cell quiescence in the adult hippocampus. Cell Rep. *28*, 1485–1498.e6.

Zhao, J., Chen, A.X., Gartrell, R.D., Silverman, A.M., Aparicio, L., Chu, T., Bordbar, D., Shan, D., Samanamud, J., Mahajan, A., et al. (2019). Immune and genomic correlates of response to anti-PD-1 immunotherapy in glioblastoma. Nat. Med. *25*, 462–469.

STAR★METHODS

KEY RESOURCES TABLE

REAGENT or RESOURCE	SOURCE	IDENTIFIER
Antibodies		
IF: chicken anti-GFP	Aves labs	Cat# GFP-1020; RRID: AB_10000240
IF: rabbit anti-c-MYC (clone D3N8F)	Cell Signaling Technology	Cat# 13987; RRID: AB_2631168
IF: rabbit anti-c-FOS (clone EPR21930-238)	Abcam	Cat# ab222699
IF: rabbit anti-ID4 (clone 82-12)	Biocheck	Cat# BCH-9/82-12; RRID: AB_2814978
IF: rabbit anti-PCNA (clone D3H8P)	Cell Signaling Technology	Cat# 13110; RRID: AB_2636979
IF: goat anti-IBA1	Novus Biologicals	Cat# NB100-1028; RRID: AB_521594
IF: rabbit anti-TMEM119 (clone 28-3)	Abcam	Cat# ab209064; RRID: AB_2800343
IF: rat anti-CD68 (clone FA-11)	Biorad	Cat# MCA1957GA; RRID: AB_324217
IF: rat anti-I-A/I-E Alexa Fluor® 647 (clone M5/114.15.2)	Biolegend	Cat# 107618; RRID: AB_493525
IF: rabbit anti-CD8α (clone EPR21769)	Abcam	Cat# ab230156
IF: rabbit anti-CD4 (clone EPR19614)	Abcam	Cat# ab183685; RRID: AB_2686917
IF: goat anti- NKp46	R&D System	Cat# AF2225; RRID: AB_355192
IF: rabbit anti- KI67	Abcam	Cat# ab15580; RRID: AB_443209
IF: rat CD3 (clone KT3)	produced in-house	N/A
IF: donkey anti-chicken Alexa Fluor® 488	Jackson ImmunoResearch	Cat# 703-545-155; RRID: AB_2340375
IF: donkey anti-rabbit Cy3	Jackson ImmunoResearch	Cat# 711-165-152; RRID: AB_2307443
IF: donkey anti-rabbit Alexa Fluor® 647	Jackson ImmunoResearch	Cat# 711-605-152; RRID: AB_2492288
IF: donkey anti-goat Cy3	Jackson ImmunoResearch	Cat# 705-165-147; RRID: AB_2307351
IF: donkey anti-goat Alexa Fluor® 647	Jackson ImmunoResearch	Cat# 705-605-147; RRID: AB_2340437
IF: donkey anti-rat Cy3	Jackson ImmunoResearch	Cat# 712-166-153; RRID: AB_2340669
IF: donkey anti-rat Cy5	Jackson ImmunoResearch	Cat# 712-175-153; RRID: AB_2340672
FC: anti-mouse/human CD11b PerCP/Cy5.5 (clone M1/70)	Biolegend	Cat# 101228; RRID: AB_893232
FC: anti-mouse CD45 Pacific Blue™ (clone 30-F11)	Biolegend	Cat# 103126; RRID: AB_493535
FC: anti-mouse CD49d PE/Cy7 (clone R1-2)	Biolegend	Cat# 103617; RRID: AB_2563699
FC: anti-mouse CD3e BV605 (clone 145-2C11)	Biolegend	Cat# 100351; RRID: AB_2565842
FC: anti-mouse CD3e PE/Cy7 (clone 145-2C11)	Biolegend	Cat# 100320; RRID: AB_312685
FC: Alexa Fluor® 647 mouse IgG2a, k isotype ctrl	Biolegend	Cat# 400234
FC: Purified anti-mouse CD16/32 (clone 93)	Biolegend	Cat# 101301; RRID: AB_312800
FC: anti-mouse I-A/I-E BV510 (clone M5/114.15.2)	Biolegend	Cat# 107636; RRID: AB_2734168
FC: anti-mouse Ly6G PE (clone 1A8)	Biolegend	Cat# 127607; RRID: AB_1186104
FC: anti-mouse Ly6C BV785 (clone HK1.4)	Biolegend	Cat# 128041; RRID: AB_2565852
FC: anti-mouse PD-1 BV421 (clone 29F.1A12)	Biolegend	Cat# 135218; RRID: AB_2561447
FC: anti-mouse ICOS BV785 (clone C398.4A)	Biolegend	Cat# 313534; RRID: AB_2629729
FC: anti-mouse CD69 PE (clone H1.2F3)	Biolegend	Cat# 104508; RRID: AB_313111
FC: anti-mouse TBX21 (TBET) PE-Cy7 (clone eBio4B10)	Thermo Fisher Scientific	Cat# 25-5825-82; RRID: AB_11042699

(*Continued on next page*)

Continued

REAGENT or RESOURCE	SOURCE	IDENTIFIER
FC: anti-mouse Tim-3 APCFire 750 (clone RMT3-23)	Biolegend	Cat# 119738; RRID: AB_2810368
FC: anti-mouse CTLA-4 APC (clone UC10-4B9)	Thermo Fisher Scientific	Cat# 17-1522-82; RRID: AB_2016700
FC: anti-mouse CD3 Alexa Fluor® 700 (clone 17A2)	Biolegend	Cat# 100216; RRID: AB_493697
FC: anti-mouse Perforin PE (clone eBioOMAK-D)	Thermo Fisher Scientific	Cat# 12-9392-82; RRID: AB_466243
FC: anti-mouse IFN-gamma PE-Cy7 (clone XMG1.2)	Biolegend	Cat# 505826; RRID: AB_2295770
FC: anti-TCRβ PE (clone H57-597)	Biolegend	Cat# 109208; RRID: AB_313431
FC: anti-Thy1.2 FITC (clone 53-2.1)	BD Pharmingen	Cat# 553004; RRID: AB_394543
FC: anti-mouse H-2kb/H-2Db Alexa Fluor® 647 (clone 28-8-6)	Biolegend	Cat# 114612; RRID: AB_492931
FC: anti- β2microglobulin (clone EP2978Y)	Abcam	Cat# ab75853; RRID: AB_1523204
FC: anti-STAT1 Phospho (Tyr701) Alexa Fluor® 647 (clone A17012A)	Biolegend	Cat# 666410; RRID: AB_2814503
FC: anti-STAT3 Phospho (Tyr705) PE (clone 13A3-1)	Biolegend	Cat# 651004; RRID: AB_2571892
FC: Alexa Fluor® 647 mouse IgG1 k isotype ctrl	Biolegend	Cat# 400136
FC: PE mouse IgG1, k isotype ctrl	Biolegend	Cat# 400140
WB: mouse βACTIN	Sigma	Cat# A5316; RRID: AB_476743
WB: rabbit RBPJ	Cell Signaling Technology	Cat# 5313; RRID: AB_2665555
WB: rabbit NOTCH1	Cell Signaling Technology	Cat# 3608; RRID: AB_2153354
WB: rabbit NOTCH2	Cell Signaling Technology	Cat#5732; RRID: AB_10693319
WB: rabbit IFNGR1	Proteintech	Cat# 10808-1-AP; RRID: AB_2121604
Depletion antibody anti-mouse CD4 (clone GK1.5, RatIgG2b)	Dialynas et al., 1983	N/A
Depletion antibody anti- mouse CD8α (clone 53-6.7, RatIgG2a,k)	Ledbetter and Herzenberg, 1979	N/A
Depletion antibody anti-mouse Thy-1 (clone T24, Rat IgG2b)	Bernstein et al., 1980	N/A
Chemicals		
7-AAD	Biolegend	Cat# 420403
B27 Supplement (50X)	Gibco	Cat# 17504044
BLZ945	MedChem Express	Cat# HY-12768/CS-3971
Collagenase type IV	Sigma-Aldrich	Cat# CA-22
DAPI	Roche	Cat# 10236276001
DMEM	Pan Biotech	Cat# P04-04510
DMEM:F-12 +GlutaMAX	Gibco	Cat# 31331-028
DMSO	Sigma	Cat# D8418
DNase I	Roche	Cat# 10104159001
EGF (recombinant human)	R&D Systems	Cat# 236EG
FBS (Lot P130914)	Pan Biotech	Cat# P40-37500
FGF2 (recombinant human)	R&D Systems	Cat# 233-FB
HBSS	Gibco	Cat# 14175053
IFNγ (recombinant mouse)	Peprotech	Cat# AF-315-05
IFNγ (recombinant human)	Peprotech	Cat# AF-300-02
L-15 Medium	Invitrogen	Cat# 31415029
Normal Donkey Serum	Jackson ImmunoResearch	Cat# 017-000-121
Paraformaldehyde	Carl Roth	Cat# 0335

(*Continued on next page*)

Continued

REAGENT or RESOURCE	SOURCE	IDENTIFIER
Papain	Sigma	Cat# P3125-100MG
Pen/Strep	Gibco	Cat# 15070063
Poly-L-lysine hydrobromide	Sigma	Cat# P9155
Sucrose	Sigma	Cat# 84100
Triton X-100	PanReac AppliChem	Cat# A4975
Trizol	Life Technologies	Cat# 15596026
True-Phosp™ Perm Buffer	Biolegend	Cat# 425401
TrypLE™ Express Enzyme	Gibco	Cat# 12604021
Trypsin 2.5% (10X)	Life Technologies	Cat# 15090046
Trypsin inhibitor Glycine max (Soybean)/ Ovomucoid	Sigma	Cat# T6522
Versene	Gibco	Cat# 15040033
Zombie Aqua™ Fixable Viability Kit	Biolegend	Cat# 423102
Critical commercial assays		
CalPhos kit	Takara	Cat# 631312
Chromium Single Cell 3' GEM, Library & Gel Bead Kit v3	10x Genomics	Cat# PN-1000075
Cytofix/Cytoperm™ kit	BD	Cat# 554714
eBioscience™ Foxp3/Transcription Factor Staining Buffer	Thermo Fisher Scientific	Cat# 00-5523
LS columns	Miltenyi Biotec	Cat# 130-042-401
Myelin Removal Beads II	Miltenyi Biotec	Cat# 130-096-731
MyTaq DNA Polymerase	Bioline	Cat# BIO-21105
Retro-X Concentrator kit	Takara	Cat# 631455
PowerUp™ SYBR™ Green Master Mix	Thermo Fisher Scientific	Cat# A25742
SsoAdvanced™ Universal Probes Supermix	Biorad	Cat# 172-5280
SuperScript IV VILO Master Mix with ezDNase Enzyme	Thermo Fisher Scientific	Cat# 11766500
TruSeq Stranded mRNA	Illumina	Cat# 20020595
Deposited data		
Bulk RNA-seq data of tumor cells at an early stage of glioma formation	This paper	GEO: GSE160715 (GSE160669)
scRNA-seq data of CD45^{+} immune cells in the tumor microenvironment	This paper	GEO: GSE160715 (GSE160714)
Human IDH mutant gliomas with Notch mutations	Bai et al., 2016	EGAS00001001588
Human persister cells	Liau et al., 2017	GEO: GSE74557
Human IDH wild-type GBM	Neftel et al., 2019	GEO: GSE131928
Human IDH mutant and 1p19q codel oligodendroglioma	Tirosh et al., 2016	GEO: GSE70630
Human IDH mutant glioma	Venteicher et al., 2017	GEO: GSE89567
Original western blot images (Figures S1D, S6D, and S6F)	Mendeley data	https://doi.org/10.17632/kkbff4wkzv.1
Experimental models: Cell lines		
Mouse: PDGF^{+}*Trp53*$^{-/-}$ glioma cell line	This paper	Control tumor cells
Mouse: PDGF^{+}*Trp53*$^{-/-}$*Rbpj*$^{-/-}$ glioma cell line	This paper	*Rbpj*$^{-/-}$ tumor cells
Human: GSC8 cell line	Wakimoto et al., 2009	N/A
Human: GSC125 cell line	Wakimoto et al., 2009	N/A
Platinum-E cells	Cell Biolabs	Cat# RV-101; RRID: CVCL_B488

(*Continued on next page*)

Continued

REAGENT or RESOURCE	SOURCE	IDENTIFIER
Experimental models: Organisms/strains		
Mouse: C57BL/6JRj	Janvier Labs	https://www.janvier-labs.com/en/fiche_produit/c57bl-6jrj_mouse/
Mouse: *Rosa26-CAG-LSL-GFP*	Tchorz et al., 2012; Giachino et al., 2015	N/A
Mouse: *Hes5::CreER*^{T2}	Giachino et al., 2015	Tg(Hes5-cre/ERT2)^{2Vtlr}
Mouse: *Trp53*$^{p/p}$	Jonkers et al., 2001	Trp53^{tm1Brn}
Mouse: *Rbpj*$^{p/p}$	Han et al., 2002	Rbpj^{tm1Hon}
Mouse: *Notch1*$^{p/p}$	Radtke et al., 1999	Notch1^{tm1Agt}
Mouse: *Notch2*$^{p/p}$	Besseyrias et al., 2007	Notch2^{tm1Frad}
Oligonucleotides and primers		
See Table S6	N/A	N/A
Recombinant DNA		
pMIG PDGF-IRES-Cre	Giachino et al., 2015	N/A
Software and algorithms		
Fiji	Schindelin et al., 2012	https://imagej.net/Fiji
FlowJo	Becton, Dickinson & Company	https://www.flowjo.com/
GO PANTHER	GENEONTOLOGY	http://geneontology.org/
GraphPad Prism 8	GraphPad	https://www.graphpad.com/scientific-software/prism/
Illustrator	Adobe	https://www.adobe.com/Illustrator
MetaCore	Clarivate Analytics	https://portal.genego.com
Omero	OME	https://www.openmicroscopy.org/about/
R studio	R Core Team, 2020	https://rstudio.com

RESOURCE AVAILABILITY

Lead contact

Further information and requests for resources should be directed to and will be fulfilled by the lead contact, Claudio Giachino (claudio.giachino@unibas.ch).

Materials availability

This study did not generate new unique reagents.

Data and code availability

- All RNA-seq data generated during this study have been deposited at GEO and are publicly available as of the date of publication. Accession numbers are listed in the key resources table. Original western blot images have been deposited at Mendeley and are publicly available as of the date of publication. The DOI is listed in the key resources table.
- This paper does not report any original code.
- Any additional information required to reanalyze the data reported in this paper is available from the lead contact upon request.

EXPERIMENTAL MODEL AND SUBJECT DETAILS

Animal models

Floxed *Rbpj*, floxed *Notch1*, floxed *Notch2*, floxed *Trp53* and *Rosa-CAG::GFP* mice have been described previously (see key resources table) (Besseyrias et al., 2007; Han et al., 2002; Jonkers et al., 2001; Radtke et al., 1999; Tchorz et al., 2012). Mice were maintained on a 12 h day/night cycle with adequate food and water under SPF conditions and according to institutional regulations under license numbers 2537, 2538, 2689 and 2929 and all experiments were approved by the ethics commission of the Kantonales Veterinäramt Basel-Stadt, Basel, Switzerland. Male and female mice were used in the analyses.

Cell Lines

PDGF^{+}*Trp53*$^{-/-}$*Rbpj*$^{-/-}$ and control (PDGF^{+}*Trp53*$^{-/-}$) tumor cell lines were generated by FACS purification of malignant cells (GFP^{+}) directly from early tumors 3 weeks after glioma induction. Gliomas were induced by intracranial injection of a retrovirus expressing PDGF-B and Cre-recombinase into floxed *Trp53* mice carrying a Cre-reporter allele (*Rosa-CAG::GFP*) to genetically label tumor cells by GFP expression *in vivo*. 3 PDGF^{+}*Trp53*$^{-/-}$*Rbpj*$^{-/-}$ and 3 control (PDGF^{+}*Trp53*$^{-/-}$) glioma cell lines were independently generated each from a different tumor and used in the experiments. Culture conditions are detailed below.

Patient-derived glioma stem cell lines (GSC8 and GSC125) were obtained from Massachusetts General Hospital (Wakimoto et al., 2009).

METHOD DETAILS

Retroviral constructs, retroviral transduction and generation of murine gliomas

For retroviral constructs, the bicistronic retroviral vector pMIG (AddGene) was used. Generation of the PDGFB-IRES-Cre retroviral vector was described previously (Giachino et al., 2015) by cloning cDNA sequences encoding human PDGFB and Cre-recombinase fused to a nuclear localization sequence (NLS) into the pMIG vector. Replication-deficient retroviruses were generated from this construct by transfecting Platinum-E cells (Cell Biolabs) using the CalPhos kit (Clontech). Retroviral supernatants were harvested after 48 h, viruses were purified using the Retro-X Concentrator kit (Clontech) following manufacturer's instructions, resuspended in TNE buffer, aliquoted and stored at -80°C until use.

Generation of murine gliomas was described previously (Giachino et al., 2015). PDGFB-IRES-Cre retroviral particles were injected into the anterior forebrain of postnatal day 1-2 mouse pups carrying floxed *Trp53* alleles, thereby simultaneously inducing PDGF overexpression and *Trp53* loss in the transduced proliferating neural progenitor cells. A Cre-reporter allele (*Rosa-CAG::GFP*) was used to genetically label tumor cells by GFP expression *in vivo*. Pups were narcotized in an atmosphere of 5% Isoflurane and then maintained in a constant flow of 1-2.5% Isoflurane in oxygen through a face mask. 1-2 μl of concentrated virus solution was injected using sharpened Borosilicate glass capillaries (Kwick-Fil) and a stereotaxic apparatus (David Kopf instruments) and the following stereotaxic coordinates relative to lambda: 3 mm rostral, 1 mm lateral, 1.5 mm below the skull. For analysis of tumors at early stages, brains were harvested 3 weeks after injection of the PDGFB-IRES-Cre virus. For analysis of later stage tumors, the mice were continually observed after injection of the virus until they developed symptoms such as lethargy, poor grooming, weight loss, or macrocephaly. Brain tissue was processed and analyzed by immunostaining as described below.

CSF-1R inhibitor administration

Stock solutions of BLZ945 (MedChem Express) were prepared at a concentration of 200 mg/ml in DMSO (Sigma). Mice were injected intraperitoneal with BLZ945 at a dose of 200 mg/kg body weight or vehicle (DMSO). For the late treatment (TAM re-education), dosing was begun at 21 days after intracranial injection of the PDGF-IRES-Cre retrovirus and mice were treated with BLZ945 6 times every second day and killed 33 days after retrovirus injection. For the early treatment (TAM depletion), dosing was begun at 3 days after intracranial injection of the PDGF-IRES-Cre retrovirus and mice were treated with BLZ945 8 times every second or third day and killed 21 days after retrovirus injection.

In vivo depletion of T lymphocytes

A mixture of 3 antibodies was used for T cell depletion *in vivo*: anti-mouse CD4 (clone GK1.5, RatIgG2b), anti-mouse CD8 alpha (clone 53-6.7, RatIgG2a,k), and anti-mouse Thy-1 (clone T24, Rat IgG2b). Mice were injected intraperitoneal with the antibody mixture (200 μg anti-CD4, 100 μg anti-CD8, 50 μg anti Thy-1 per mouse) or vehicle (phosphate-buffered saline, PBS). Dosing was begun at 3 days after intracranial injection of the PDGF-IRES-Cre retrovirus and mice were treated with depletion antibodies 7 times every second or third day and killed 21 days after retrovirus injection.

Successful depletion of T lymphocytes was confirmed by flow cytometry analysis of lymph nodes. Inguinal and axillary lymph nodes were mechanically dissociated and the cell suspension was stained in PBS + 2% fetal calf serum with anti-TCR, anti-Thy1.2, anti-CD4 and anti-CD8α antibodies and analyzed on a CytoFLEX Flow Cytometer (Beckman Coulter). Analysis of flow cytometry data was performed with FlowJo (BD).

Immunostaining of brain tissue and cell cultures

For histology, mice were deeply anaesthetized by injection of a ketamine/xylazine/acepromazine solution (130 mg, 26 mg and 4 mg/kg body weight, respectively) and perfused with ice-cold 0.9% saline solution followed by ice-cold 4% paraformaldehyde (PFA) solution in 0.1 M phosphate buffer (PB). Brains were post-fixed with 4% PFA overnight, washed in PB, cryoprotected in a 30% sucrose solution in 0.1 M PB for 48 h, embedded and frozen in OCT (TissueTEK). Free floating coronal sections (30 μm) were collected in multi-well dishes (Corning) and stored at -20°C in anti-freeze solution until use.

For immunostaining, sections were incubated overnight either at 4°C or room temperature with the primary antibody diluted in blocking solution of 2% normal donkey serum (Jackson ImmunoResearch), 0.5% Triton X-100 (AppliChem) in PBS. Sections were washed three times in PBS and incubated at room temperature for 1 h and 40 min with the corresponding secondary antibodies in blocking solution. When necessary, sections were counter-stained with DAPI (1 μg/ml). For PCNA detection, antigen

was recovered at 80°C for 20 min in Sodium Citrate solution (10 mM, pH 6). For c-MYC detection, antigen was recovered at 85°C for 30 min in Tris-EDTA Buffer (10mM Tris Base, 1mM EDTA, 0.05% Tween 20, pH 9).

Cell cultures were fixed with pre-warmed 4% PFA for 10 min at room temperature, washed, and incubated overnight at 4°C with primary antibodies diluted in blocking solution of 10% normal donkey serum, 1% bovine serum albumin (BSA), 0.2% Triton X-100 in PBS.

Stained sections and coverslips were mounted on glass slides (VWR, or Superfrost by Thermo Scientific), embedded in mounting medium containing diazabicyclo-octane (DABCO, Sigma) as an anti-fading agent and visualized using either a Leica TSC SP5 confocal microscope or a Zeiss Observer.Z1 equipped with Apotome. The antibody information is described in the key resources table.

Tumor isolation, fluorescence activated cell sorting (FACS) and flow cytometry

Glioma cells and immune cells from the tumor microenvironment (TME) of early-stage gliomas were purified by FACS 3 weeks after injection of the PDGFB-IRES-Cre virus into the mouse brain. Murine gliomas (GFP^+, *Rosa-CAG::GFP* Cre-reporter allele, see above) were identified by inspection of the brain under a fluorescent stereomicroscope (MZFLIII, Leica), carefully resected, and minced into small pieces in ice cold L15 medium (GIBCO) with the help of a scalpel. The tissue was then digested with a Papain solution (Sigma) for 10 min at 37°C, followed by 15 min at 37°C in a Papain / Trypsin inhibitor (Sigma) mix and then washed two times in PBS. When necessary, cells were incubated with fluorophore-conjugated antibodies for 30 min at 4°C in PBS + 0.5% BSA + 2mM EDTA. Cells were resuspended in PBS + 2mM EDTA, stained for viability with 7-aminoactinomycin D (7-AAD) or Propidium Iodide (PI), and immediately sorted.

For Papain-sensitive T cell activation markers, tumors were dissociated in 0.5 mg/ml Collagenase IV and 40μg/ml DNase at 37°C with shaking at 200rpm for 30 min. The cell suspension was then washed and passed through a 70μm cell strainer. Myelin debris was removed by incubating the cell suspension with 20μl of Myelin Removal Beads (Miltenyi) at 4°C for 15 min and using LS columns (Miltenyi) following manufacturer's instructions. Cells were incubated with antibodies for cell surface markers for 30 min at 4°C in PBS + 0.5% BSA and with a fixable live/dead stain (Zombie Aqua, Biolegend), then fixed and stained for intracellular markers for 30 min at 4°C in PBS + 0.5% BSA. Fixation was performed using the eBioscience™ Foxp3/Transcription Factor Staining Buffer Set (Thermo Fisher Scientific) for TBX21 staining or the BD Cytofix/Cytoperm™ Fixation/Permeabilization kit (BD) for cytokines staining. All antibodies were titrated and tested for compatibility with the dissociation protocols. Antibody details are listed in the key resources table. Cell sorting was performed on a FACS AriaIII (BD) using FACS Diva (BD). Flow cytometry acquisition was performed on a CytoFLEX Flow Cytometer (Beckman Coulter). Analysis of flow cytometry data was performed with FlowJo (BD).

GSCs and microglia cell cultures

Murine glioma cell lines were generated by FACS purification of malignant cells directly from early tumors as described above. Glioma cells were maintained as floating tumorspheres in T25 cell culture flasks (CELLSTAR) containing DMEM-F12+Glutamax (Gibco) + 2% B27 (Gibco) + 10 ng/ml EGF (R&D) + 20 ng/ml FGF (R&D) + 1% penicillin/streptomycin (Gibco) and split every 4-5 days. Cells were grown under standard conditions (21% O_2 and 5% CO_2) at 37°C. For proliferation assays glioma cells were maintained as adherent cultures in 100 μg/ml Poly-L-Lysine (Sigma)-coated glass coverslips (VWR). Cells were treated with 1 ng/ml, 10 ng/ml, or 100 ng/ml IFNγ (Peprotech) for the indicated amount of time.

For quantification of cell death after IFNγ treatment, cells were dissociated, incubated with 7-AAD solution for 10 min and analyzed with a CytoFLEX Flow Cytometer (Beckman Coulter).

For conditioned medium (CM) generation, early-passage (2-3) primary glioma cells were seeded at a concentration of 2.5 x 10^4 cells/ml into T25 cell culture flasks in complete medium. 5 days after plating the supernatants were harvested, centrifugated (100g for 5 min), filtered (0.22μm filters, Membrane Solutions) to remove debris and stored at -80°C until further use.

Cre-dependent deletion of floxed Notch alleles was confirmed by genotyping. To extract the DNA, acutely isolated GFP^+ tumor cells were incubated in digestion buffer (50mM KCl, 10mM Tris-HCl pH 9, 0.1% Triton X-100, 0.4 mg/ml Proteinase K) at 60°C for 3h. PCRs were performed using a MyTaq DNA Polymerase (Bioline). Details of primers are listed in the key resources table.

Patient-derived glioma stem cell lines (GSC8 and GSC125) were obtained from Massachusetts General Hospital. Cell were maintained in serum-free medium containing EGF (20 ng/ml) and FGF (20 ng/ml) as previously described (Wakimoto et al., 2009).

Primary microglia cells were isolated from postnatal day 1-2 mouse pups and cultures prepared. Briefly, mixed glial cultures were prepared from the cerebral cortex and cultured in high glucose (4.5 g/L) DMEM+GlutaMax (Pan Biotech) + 10% fetal bovine serum (Pan Biotech) + 1% penicillin/streptomycin (Gibco) for 10-14 days changing half of the medium every 3 days. Microglia cells were then harvested by orbital shaking at 120 rpm for 2 h. Isolated microglia cells were re-seeded onto Poly-L-Lysine (Sigma)-coated 96-well plates (Falcon) at a density of 3 x 10^4 cells/well and let recover for 24 h at 37°C, 5% CO_2, 21% O_2. Half of the medium was then replaced with CM from tumorspheres and cells were fixed 72 h later. Morphological analysis of individual microglia cells was done using Image J software (v2.1.0). Technical duplicates of each experiment condition were obtained. The experiment was repeated three times and every time CM from 2 different glioma cell lines was used, for a total of 250-350 microglia cells analyzed per condition.

For transwell assays, glioma cells were plated as adherent cultures in 24-well plates (Falcon) at a density of 4 x 10^4 cells/well and cultured for 3 days. Cell culture inserts with 8 μm pore size (Falcon) were added to each well and 5 x 10^4 microglia cells were seeded on top of the membrane and cultured at 37°C under standard conditions for 6-12 h. Transwells were fixed and stained with DAPI following manufacturer's instructions and the entire membrane was imaged with a Zeiss Observer.Z1 microscope equipped with

Apotome. Cells were automatically counted using Image J software (v2.1.0) using the Analyze Particles function. Technical duplicates of each experiment condition were obtained. The experiment was repeated twice and each time 2 different glioma cell lines were used.

For phagocytosis assays *in vitro*, microglia cells were plated into ultra-low attachment round-bottom 96-well plates (Costar) at a density of 5 x 10^4 cells/well and allowed to recover for 1 h at 37°C. Glioma cells were dissociated to a single-cell suspension with Trypsin (Gibco) for 5 min at 37°C and added to microglia at a density of 1 x 10^5 cells/well. Microglia and glioma cells were co-cultured (final ratio 1:2) in serum- and growth factors-free DMEM-F12 for 2 h at 37°C and then stained with an anti-CD11b antibody to identify microglia cells, while glioma cells were identified by GFP expression. Cells were analyzed with CytoFLEX Flow Cytometer (Beckman Coulter) using a high throughput sampler. Technical duplicates of each experiment condition were obtained. The experiment was repeated twice and every time 3 different glioma cell lines were used.

Total cell protein extraction and western blotting

Cells were washed once in ice-cold PBS and then lysed on ice for 30 min in a modified Ripa buffer containing 50mM Tris (pH 8.0), 150mM NaCl, 0.5mM MgCl2, 0.5mM EDTA, 1% Triton- X and 0.5% SDS supplemented with Complete Protease Inhibitors cocktail (Roche) and phosphatase inhibitors (20mM sodium fluoride, 1mM sodium orthovanadate). Cell lysates were sonicated using a Bioruptor (Diagenode) and centrifugated at 12000 rpm for 20 min at 4°C. For determination of total protein concentration, the BCA Protein Assay Kit (Thermo Fisher) was used according to manufacturer's instructions. 5x Laemmli Buffer was added to the samples to reach a final volume of 1x and heated 5 min at 95 °C. Equal concentrations (20-40μg) of total cell extracts were separated on 8% SDS polyacrylamide gels and transferred to nitrocellulose membranes (Protran). The membrane was blocked with 5% milk in TBS-T for 1 h, followed by overnight incubation with antibody in blocking buffer at 4°C. The membrane was washed three times for 5 min with TBS-T followed by incubation with HRP-conjugated secondary antibody in 5% milk in TBS-T for 1 h at room temperature. The membrane was then washed three times with TBS-T and twice with TBS. Protein expression was detected on medical X-Ray films using the Pierce™ ECL Western Blotting Substrate (Thermo Fisher). Relative protein expression was normalized to β-ACTIN expression levels.

Phosphoflow cytometry

Phosphoflow cytometry was adapted from previous published protocols. Briefly, GSCs were stimulated with IFNγ (mouse or human) for 10 minutes at 37°C and immediately placed on ice, washed, and spun down at 4°C. Tumorspheres were then dissociated with Papain solution followed by Papain / Trypsin inhibitor mix (murine spheres) or TrypLE (human spheres) and fixed with 1.6% prewarmed PFA for 10 minutes at 37°C. Cell were then centrifuged, washed with PBS + 1% BSA + 2mM EDTA to remove residual PFA, and permeabilized with ice-cold True-Phos™ Perm Buffer (Biolegend) for 2h at -20°C. After 2 washes with PBS + 1% BSA + 2mM EDTA, cells were incubated with primary antibody in the same washing buffer for 30 minutes at 4°C in the dark. Cells were resuspended in PBS + 2mM EDTA and analyzed with CytoFLEX Flow Cytometer (Beckman Coulter).

RNA isolation and quantitative reverse-transcriptase PCR

Total RNA was isolated using Trizol (Life Technologies) and a standard phenol-chloroform protocol following manufacturer's instructions with some modifications. 1ml of Trizol (Life Technologies) was added to the sample, followed by 20% of total volume chloroform. Samples were centrifuged at 12'000 x g for 30 min at 4°C. The aqueous phase was extracted, RNA was precipitated overnight with isopropanol and 15μg of GlycoBlue (Invitrogen) at -20°C, and then washed with 75% ethanol. The RNA pellet was resuspended in RNase-free Milli-Q water. Reverse transcription was performed using SuperScript™ IV VILO™ (Thermo Fischer) following manufacturer's instructions after genomic DNA digestion with ezDNAse enzyme (Thermo Fisher) for 5 min at 37°C. Quantitative reverse-transcriptase PCR was performed using the SsoAdvanced Universal Probes Supermix (Bio-Rad) and the Universal Probe Library System Assay (Roche) or the PowerUp™ SYBR Green Master Mix (Thermo Fisher Scientific) and run on a qTOWER^3 real-time PCR machine (Analytik Jena). Details of primers and probes are listed in the key resources table. Relative gene expression was normalized to *Rpl13a* or *Tbp* expression levels. RNA expression data are presented as normalized expression (2^{-dCt}) using the Ct method. 3 technical replicates and 3 biological replicates for each gene were analyzed.

RNA-seq

Bulk RNA-seq

4-6 independent samples per each tumor genotype (PDGF$^+$*Trp53*$^{-/-}$*Rbpj*$^{-/-}$, PDGF$^+$*Trp53*$^{-/-}$*Notch1*$^{-/-}$*Notch2*$^{-/-}$, PDGF$^+$*Trp53*$^{-/-}$*Notch1*$^{-/-}$, PDGF$^+$*Trp53*$^{-/-}$*Notch2*$^{-/-}$, and control PDGF$^+$*Trp53*$^{-/-}$ tumor) were analyzed by RNA-seq. Each sample included a pool of tumor cells from 1-5 different tumors. Early-stage (3 weeks) gliomas were identified by the expression of GFP from the *Rosa-CAG::GFP* Cre-reporter, micro-dissected, and GFP$^+$ tumor cells purified by FACS as described above. RNA was isolated using TRIzol (Invitrogen) as described above. TruSeq stranded mRNA libraries (Illumina) were generated and sequencing was performed on a NextSeq 500 (Illumina). Reads were mapped to the mouse genome (mm10 version downloaded from UCSC) using STAR aligner (v 2.5.2a) with default parameters except for allowing up 10 hits to genome (outFilterMultimapNmax 10), reporting only one location for hits with equal score (outSAMmultNmax 1), and for filtering reads without evidence in spliced junction table (outFilterType "BySJout"). Gene expression level was estimated as the number of reads that started within any annotated exon of a gene using RefSeq mRNA coordinates from UCSC (genome.ucsc.edu, downloaded in December 2015) and the qCount function from QuasR package. Between samples normalization

was done using the TMM method. Differentially expressed genes were identified using the framework of generalized linear models (GLM) implemented in package edgeR. GLM was fitted to the raw counts (glmFit) and differences between experimental groups were tested with likelihood ratio test (glmLRT). P-values were adjusted by controlling the false discovery rate (FDR; Benjamini-Hochberg method) and genes with a FDR lower than 5% were considered significant. For the clustering analysis, samples were clustered using 25% of most variable genes across the dataset, applying hclust function with default "complete" method and using (1-Pearson correlation) as a distance measure.

Single cell RNA-seq

CD45$^+$ immune cells from pools of 9 healthy brains, 9 PDGF$^+$*Trp53*$^{-/-}$*Rbpj*$^{-/-}$ tumors and 15 control (PDGF$^+$*Trp53*$^{-/-}$) tumors were purified by FACS as described above and analyzed by scRNA-seq. To circumvent potential batch effects, two independent sample replicates per each of the three conditions (healthy brain, PDGF$^+$*Trp53*$^{-/-}$*Rbpj*$^{-/-}$ tumor, control PDGF$^+$*Trp53*$^{-/-}$tumor) were analyzed. Single cell capture and library preparation were performed with a Single Cell 3' v3 Kit (10x Genomics). Sequencing was performed on a Illumina NovaSeq 6000 according to 10x specifications (R1 read 28nt (16+12), R2 read 91nt). Read quality was assessed with the FastQC tool (version 0.11.5). Kallisto (version 0.46.0) and BUStools (version 0.39.3) were used to perform cell demultiplexing and to pseudo-align reads to mouse transcripts derived from Ensemb version 97 and to their intronic regions (extended on each side by 90nt). The series of commands ''bustools correct'', ''bustools capture'' and ''bustools count'' were applied to generate gene-level spliced and unspliced UMI counts tables. Processing of the UMI count matrix for transcripts was done according to the steps illustrated in Bioconductor Single Cell Analysis workflow. The final filtered and normalized (with deconvolution-based size factors) expression matrix contained data for 27378 genes in 17362 cells. The R version 4.0.0 and the packages from Bioconductor (version 3.1) were used for downstream analysis (DropletUtils 1.8.0, scran 1.16.0, scater 1.16.2, SingleCellExperiment 1.10.1, SingleR 1.2.4, limma 3.44.3, edgeR 3.30.3, irlba 2.3.3)). Clustering of cells was done on normalized log-count values using a hierarchical clustering and the partitioning of the dendrogram was obtained with cutreeDynamic function (dynamicTreeCut 1.63.1). Key marker genes specifically expressed in each of the clusters were identified with findMarkers function from scran package (1.16.0).

For some analyses, cells from each condition (healthy brain, PDGF$^+$*Trp53*$^{-/-}$*Rbpj*$^{-/-}$ tumor, control PDGF$^+$*Trp53*$^{-/-}$ tumor) from the MG/MDM population or T cell population were aggregated into *in silico*-bulk samples (Lun and Marioni, 2017). Differential expression analysis across tumor types was done within the edgeR framework described earlier. Differential abundance of cells expressing T cell markers, *Tbx21*, or *Ifng* was tested with Fisher's-exact test after classifying the cells as either expressing (having at least 1 UMI assigned to the gene of interest) or not-expressing a particular gene. The gene signature for homeostatic microglia was taken from the top 40 microglia-specific genes list in Butovsky et al. (2014). The immunosuppressive gene signature and the T cells activation gene signature were taken from Azizi et al. (2018), and only genes differentially expressed in our gene sets are shown.

Switch analysis

Samples were ordered from the least to the most aggressive tumor genotype (control PDGF$^+$*Trp53*$^{-/-}$ tumor < PDGF$^+$*Trp53*$^{-/-}$*Notch2*$^{-/-}$ < PDGF$^+$*Trp53*$^{-/-}$*Notch1*$^{-/-}$ < PDGF$^+$*Trp53*$^{-/-}$*Notch1*$^{-/-}$*Notch2*$^{-/-}$ ≈ PDGF$^+$*Trp53*$^{-/-}$*Rbpj*$^{-/-}$) and ranked based on canonical, Rbpj-dependent Notch signaling. All possible combinations of peak/switch models were fitted to the expression of individual genes with the GLM framework in the edgeR package. For each gene, the best-fitting model was selected, and the gene was assigned to the corresponding category. All genes with a FDR <0.05 and a log2FC >1 were classified as peak/switch genes.

Gene pathways enrichment analyses

GO enrichment analysis of the significantly differentially regulated genes (log_2FC > 1 or < -1 and FDR < 0.05) between Notch-knockout tumor cell and control tumor cells was conducted using Panther (Ashburner et al., 2000).

For GSEA, Correlation Adjusted MEan RAnk gene set test (CAMERA function from limma package) was used to estimate over-representation of genes in Hallmark curated gene sets from the MSigDB database (version 6.0 converted to mouse identifiers using homolog mapping from biomart, Ensembl version 88).

The Ingenuity Upstream Regulator analyses were generated using IPA (QIAGEN Inc., https://www.qiagenbio-informatics.com/products/ingenuity-pathway-analysis).

Analysis of human glioma datasets

Only malignant cells from scRNA-seq data (SmartSeq2, GSM3828672) (Neftel et al., 2019) were used in the analysis. First, four pseudo-bulk samples were formed with average expression profiles of cells falling into the corners in the orginal tSNE figure (corresponding to OPC-like, NPC-like, AC-like, or MES-like cells) and then each cell in the dataset was annotated using the SingleR package with one of those four labels. Normalized log TPM values were gene-centered and averaged for each selected pathway. Pearson correlation coefficients of average log fold changes across cells (either in the complete dataset, or in one of the four subsets) were visualized in the heatmaps.

Individual cells from GSE89567 dataset (Venteicher et al., 2017) were annotated using AUCell (v 1.10.0) with the lists of genes specific for ''Oligo-program", "Astro-program", "Stemness-program". Normalized log TPM values were gene-centered and averaged for each selected pathway. Pearson correlation coefficients of average log fold changes across cells (either in the complete dataset, or in one of the three subsets) were visualized in the heatmaps.

The cells from GSE70630 dataset (Tirosh et al., 2016) were annotated using AUCell (v1.10.0) with gene lists specific for ''Stemness", "AC (PCA+mice)", "OC (OG+mice)''. Normalized log TPM values were gene-centered and averaged for each selected

pathway. Pearson correlation coefficients of average log fold changes across cells (either in the complete dataset, or in one of the three subsets) were visualized in the heatmaps.

RNA-seq data from GSE74557 (Liau et al., 2017) were remapped to human genome version hg38 with STAR aligner (v 2.7.0c) with default parameters except for allowing up to 10 hits to the genome (outFilterMultimapNmax 10), reporting only one location for hits with equal score (outSAMmultNmax 1), and for filtering reads without evidence in spliced junction table (outFilterType "BySJout"). Gene expression level was estimated as the number of reads that started within any annotated exon of a gene using the rsubread:: featureCounts function and gene annotation from ensemble v96. Normalized log CPM values (TMM normalization) were gene-centered and averaged for each selected pathway. The obtained average log fold changes across samples were visualized in the heatmap. Rotation gene set test as implemented in function fry (edgeR package v3.30.3) were used to test difference in expression for selected pathways between GSC8 ''naïve'' and ''persister'' cells.

Illumina microarray data (IDAT files) from EGAS00001001588 (Bai et al., 2016) were imported into R and quantile normalized. Only one probe with highest IQR value per NCBI Gene ID was retained for further analysis. Rotation gene set test as implemented in function fry (limma package v3.44.3) were used to test difference in expression for selected pathways between Notch mutant and Notch wild-type gliomas.

Tumor-associated immune cells in TCGA GBM samples (Agilent G4502A) were inferred using the ESTIMATE method (Yoshihara et al., 2013). The GBM samples were split based on expression of the Notch target genes *HEY1*, *HEY2*, and *HES5* into "high" and "low" categories (defined as having expression of all three genes simultaneously above or below their mean expression in GBM). For MDMs and MG, the lists of gene symbols provided in Table S2 from Bowman et al. (2016) were converted to human ensembl gene IDs using biomart service (https://m.ensembl.org/biomart/martview/, v104). The genes specifically expressed in $CD4^+$ T cells and $CD8^+$ T cells were selected from Table S3 from Monaco et al. (2019) by having "FoldChange TPM_TMM" > 1 and FDR TPM_TMM < 0.0001 according to the original ESTIMATE approach (Yoshihara et al., 2013). The obtained gene lists were fed into the ESTIMATE Score function from ESTIMATE package (1.0.13) (Yoshihara et al., 2013), with minor modification to allow usage of custom gene lists. The ESTIMATE scores from high and low categories were compared with Wilcoxon Rank Sum Test (stats package, R version 4.1.0).

QUANTIFICATION AND STATISTICAL ANALYSIS

Quantifications of stained cells are presented either as average percentages of co-labeled cells or densities of cells per mm^2. Mean fluorescence intensity per field was calculated using Image J software (v2.1). 2-4 sections in at least 3 animals were quantified. For cell cultures 2-3 coverslips/wells were quantified per condition.

Statistical comparisons were conducted by Log-rank (Mantel-Cox) test (survival data), Fisher's-exact test, two-tailed unpaired Student's t test, one sample t test, or ANOVA with appropriate post-hoc test using GraphPad Prism 8. When appropriate, statistical comparisons were conducted on $\log_2$ transformed data (for ratios) or data converted by arcsine square root transformation (for percentages). Significance was established at $p < 0.05$ or FDR < 0.05. In all graphs, error bars are standard error of the mean.